Bioactive Materials 27 (2023) 377–393

Contents lists available at ScienceDirect

Bioactive Materials

journal homepage: www.keaipublishing.com/en/journals/bioactive-materials

Bioprinted constructs that simulate nerve–bone crosstalk to improve microenvironment for bone repair

Tianchang Wang [a,1], Wentao Li [b,c,1], Yuxin Zhang [d,1], Xiang Xu [a], Lei Qiang [e], Weiqiang Miao [a], Xiaokun Yue [a], Xin Jiao [a], Xianhao Zhou [a], Zhenjiang Ma [a], Shuai Li [f], Muliang Ding [g], Junfeng Zhu [i], Chi Yang [d], Hui Wang [h], Tao Li [i,***], Xin Sun [a,**], Jinwu Wang [a,h,*]

[a] *Shanghai Key Laboratory of Orthopedic Implant, Department of Orthopedic Surgery, Shanghai Ninth People's Hospital, Shanghai Jiao Tong University School of Medicine, No. 639 Zhizaoju Road, Shanghai, 200011, China*

[b] *Sports Medicine Department, Beijing Key Laboratory of Sports Injuries, Peking University Third Hospital, No.49, North Garden Road, Haidian District, Beijing, 100191, China*

[c] *Peking University Institute of Sports Medicine, No.49, North Garden Road, Haidian District, Beijing, 100191, China*

[d] *Department of Oral Surgery, Shanghai Ninth People's Hospital, Shanghai Jiao Tong University School of Medicine, College of Stomatology, Shanghai Jiao Tong University, National Center for Stomatology, National Clinical Research Center for Oral Diseases, Shanghai Key Laboratory of Stomatology, Shanghai, 200011, China*

[e] *School of Materials Science and Engineering, Southwest Jiaotong University, Chengdu, 610031, China*

[f] *Department of Orthopedics, The First Affiliated Hospital, Zhejiang University School of Medicine, 79 Qingchun Rd, Hangzhou, 310003, China*

[g] *Department of Orthopaedics, The Second Xiangya Hospital, Central South University, Changsha, 410001, Hunan, China*

[h] *Institute of Rehabilitation Medicine, School of Rehabilitation Science, Shanghai University of Traditional Chinese Medicine, Engineering Research Center of Traditional Chinese Medicine Intelligent Rehabilitation, Ministry of Education, Shanghai, 201210, China*

[i] *Department of Orthopedic Surgery, Xin Hua Hospital Affiliated with Shanghai Jiao Tong University School of Medicine, No. 1665, Kongjiang Road, Shanghai, 200092, China*

ARTICLE INFO

Keywords:
Schwann cells
Microenvironment
Nerve–bone crosstalk
Exosomes
Bioprinting

ABSTRACT

Crosstalk between nerves and bone is essential for bone repair, for which Schwann cells (SCs) are crucial in the regulation of the microenvironment. Considering that exosomes are critical paracrine mediators for intercellular communication that exert important effects in tissue repair, the aim of this study is to confirm the function and molecular mechanisms of Schwann cell-derived exosomes (SC-exos) on bone regeneration and to propose engineered constructs that simulate SC-mediated nerve–bone crosstalk. SCs promoted the proliferation and differentiation of bone marrow mesenchymal stem cells (BMSCs) through exosomes. Subsequent molecular mechanism studies demonstrated that SC-exos promoted BMSC osteogenesis by regulating the TGF-β signaling pathway via let-7c-5p. Interestingly, SC-exos promoted the migration and tube formation performance of endothelial progenitor cells. Furthermore, the SC-exos@G/S constructs were developed by bioprinting technology that simulated SC-mediated nerve–bone crosstalk and improved the bone regeneration microenvironment by releasing SC-exos, exerting the regulatory effect of SCs in the microenvironment to promote innervation, vascularization, and osteogenesis and thus effectively improving bone repair in a cranial defect model. This study demonstrates the important role and underlying mechanism of SCs in regulating bone regeneration through SC-exos and provides a new engineered strategy for bone repair.

Peer review under responsibility of KeAi Communications Co., Ltd.

* Corresponding author. Shanghai Key Laboratory of Orthopedic Implant, Department of Orthopedic Surgery, Shanghai Ninth People's Hospital, Shanghai Jiao Tong University School of Medicine, No. 639 Zhizaoju Road, Shanghai, 200011, China.

** Corresponding author.

*** Corresponding author.

E-mail addresses: litaoxyeyy@sina.com (T. Li), sunxinspine@sina.com (X. Sun), wangjw-team@shsmu.edu.cn (J. Wang).

[1] T.W. and W.L. and Y.Z. contributed equally to the work.

https://doi.org/10.1016/j.bioactmat.2023.02.013

Received 3 November 2022; Received in revised form 10 January 2023; Accepted 13 February 2023

1. Introduction

Although considerable progress has been made in the field of bone tissue engineering, the problem of repairing critical bone defects brought on by trauma, infection, or malignant resection has not yet been fully resolved [1]. Bone repair is a complex, well-orchestrated physiological process that is regulated by a combination of multiple biochemical and physical cues in the microenvironment [2]. Bone is richly innervated by nerves, and the nervous system also plays a significant part in responding to bone tissue injury [3]. Numerous studies have shown that after bone injury, the nerve first responds and regulates the bone regeneration microenvironment [4,5]. The interaction of nerves, blood vessels, immune cells, and stem cells produces a microenvironment that is conducive to bone regeneration, which is crucial for bone repair [6,7]. However, in bone tissue engineering, the vital role of nerves in the bone regeneration microenvironment is often ignored.

At present, many studies have described the mechanism of neurons regulating the bone regeneration microenvironment [8,9]. Neurotransmitters, neuropeptides, and neurotrophins secreted by neurons can improve the bone regeneration microenvironment [10,11]. Our earlier research has also shown that improving scaffold innervation strengthens effective bone repair, indicating that the regulatory effects of the nervous system in the bone regeneration microenvironment are pivotal in bone repair [12]. Schwann cells (SCs) are the primary cells in the peripheral nervous system responsible for the maintenance of the peripheral nervous system and innervation of new bone [13]; however, increasing studies have revealed that SCs themselves are crucial for regulating the microenvironment for bone repair [14]. Johnston et al. found that impaired regeneration of bone tissue was associated with the shortage of SCs [15]. Jones et al. further confirmed that the lack of regulation from SCs due to denervation caused the functional deficiency of skeletal stem cells and thus impaired bone healing [16]. Therefore, the bone regeneration effect may be enhanced by simulating the function of SCs in the microenvironment. However, the mechanism by which SCs regulate the bone regeneration microenvironment remains unclear.

Exosomes are a type of extracellular vesicle with a diameter of 30–200 nm secreted from the inside of cells through the multivesicular endosomal pathway [17]. They are composed of phospholipid bilayers, proteins, and nucleic acids and are essential in intracellular communication and information exchange [17,18]. Exosomes are an important mode of communication between cells and are crucial in regulating cells for immunity and tissue repair by transferring enriched miRNAs [19–21]. Schwann cell-derived exosomes (SC-exos) are essential for SCs to promote axonal growth and regeneration [22,23]. Wu et al. used SC-exos to enhance the biological activity of porous Ti6Al4V scaffolds to promote the regeneration and repair of bone [24]. Su et al. created a biomimetic periosteum loading SC-exos to enhance nerve repair for angiogenesis and bone regeneration [25]. Hao et al. developed a multifunctional neuromodulation platform utilizing SC-exos that improved bone repair by regulating immunomodulation, angiogenesis, and osteogenesis [26]. These studies demonstrate that SC-exos are crucial paracrine signaling agents for SCs to regulate tissue repair and that the regulatory effects of SCs for bone repair in the microenvironment can be simulated via SC-exos. However, this hypothesis needs to be further verified, and the underlying molecular regulatory mechanisms need to be explored.

In recent years, 3D bioprinting technology has been extensively used in bone tissue engineering as an advanced biofabrication technology. Bioprinting can simultaneously print high-density living cells, biomaterials, and bioactive substances, thereby enabling the assembly of structures with high biological activity [27–29]. Moreover, the bioprinted structures can create the optimal microenvironment as required by the cells, such as constructing personalized structures with multiple channels, loading bioactive substances, and facilitating the communication between cells and between the cells and the microenvironment to produce tissues and organs with biological functions [29,30]. To enhance the regulatory effects of SCs in bone repair, SC-exos and bone marrow mesenchymal stem cells (BMSCs) are loaded in the bioink, and SC-mediated nerve–bone crosstalk is stimulated to improve the microenvironment and thus promote bone regeneration. Meanwhile, an appropriate bioink should be selected to ensure that the exosome-loaded constructs can perform their functions effectively. Silk methacrylate (SilMA) is a photo-crosslinked hydrogel based on silk fibroin, which is widely applied in bone tissue engineering owing to its tunable mechanical properties, flexibility, biocompatibility, and osseointegration [31–34]. Silk can serve as a carrier for the delivery and sustained release of enzymes, drugs, and growth factors [35,36]. Studies have confirmed that silk fibroin can be used as a carrier for exosomes, maintaining the biological activity of exosomes for a long time and releasing them slowly [37,38]. Thus, a hybrid hydrogel system was used as a bioink in this study, where thermosensitive gelatin methacrylate (GelMA) was used as the base of the hybrid hydrogel and SilMA was added to improve the release manner of exosomes.

In this research, we established the preliminary molecular mechanism of SCs as the main cellular components of the peripheral nervous system to regulate the microenvironment through exosomes to promote bone regeneration (Fig. 1A). We then developed the SC-exos loaded bioprinted constructs that simulate the effects of SCs to improve the microenvironment and thus enhance the bone repair effect. Particularly, as shown in Fig. 1B, BMSCs and SC-exos were added to GelMA and SilMA hybrid hydrogel as the bioink, and the constructs were fabricated by bioprinting technology. The bioprinted constructs can potentially promote the osteogenic differentiation of BMSCs by simulating SC-mediated nerve–bone crosstalk (Fig. 1C). In addition, we hypothesized that the release of SC-exos would improve the bone regeneration microenvironment and further stimulate the neurovascular network formation, which would ultimately complete the neurovascularized bone repair (Fig. 1D).

2. Results

2.1. SCs are involved in the bone repair process

SCs are considered to be a pro-regenerative cell type in the peripheral nervous system, dedifferentiating into repair-SCs after injury. They not only promote the regeneration of the nerves but also of other tissues, such as the heart, skin, and bone [16,39–41]. Itoyama et al. found that SCs increased in number in damaged rat periodontal tissue during the total healing process and played a vital part in the healing of alveolar bone tissue [42]. Here, to verify whether SCs were involved in the process of bone repair, we investigated the immunofluorescence expression of S100β, which belonged to the SC special markers, in bone tissue near the fracture of the rat femur at 3, 7, and 14 d. The β III-tubulin, a specific marker of nerve axons, was also stained to observe the distribution of nerve fibers. Normal bone tissue was used as the control. As seen in Fig. 2A, the reports of S100β signal were hardly noticeable in the uninjured area of bone tissue. Only a weak S100β report could be observed in the periosteum. However, as shown in the following Fig. 2B, some positive reports of S100β signal could be observed in the callus of fracture at 3 d post-fracture. Thereafter, numerous positive reports of S100β signal were observed in the callus of fracture at 7 d post-fracture (Fig. 2C). And the number of S100β-positive cells was further increased at 14 d post-fracture (Fig. 2D). Nerve fibers are mainly distributed in the periosteum and surrounding muscle tissue. This result was consistent with most reports that nerve fibers were mainly distributed in the periosteum [43,44]. The results of the quantitative analysis of immunofluorescence intensity of S100β expression in uninjured and injured bone tissue were shown in Fig. S1. This finding suggested that SCs at the injury site proliferated dramatically post-fracture, entered the callus, and participated in the process of fracture repair, which was consistent with previous findings. Itoyama et al. reported that S100β-immunoreactive cells could be detected in the

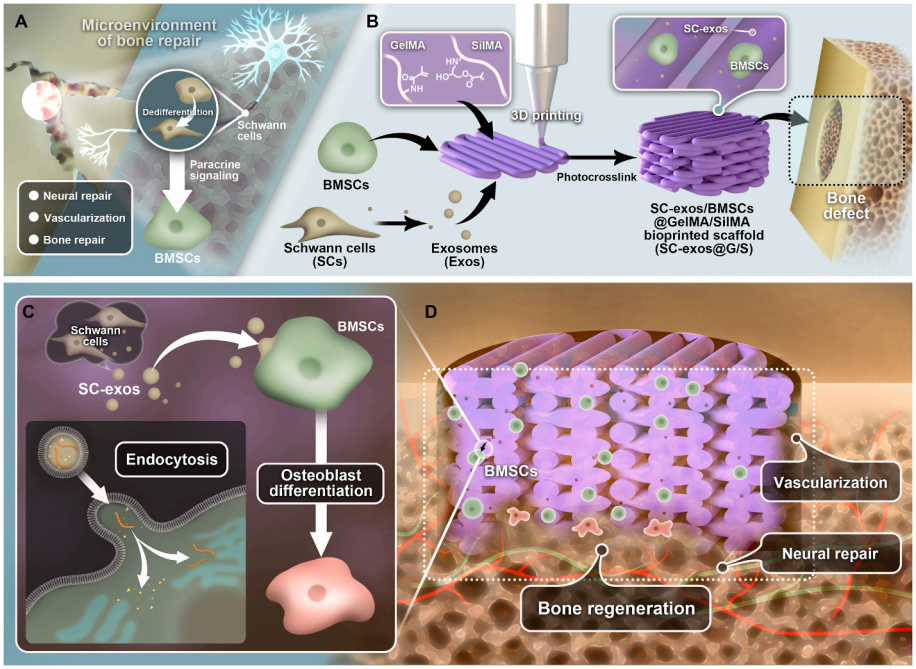

Fig. 1. (A) Schematic showing that SCs from the peripheral nervous system participate in the regulation of the bone regeneration microenvironment and bone repair through paracrine actions. (B) Schematic illustrating the procedures used to cross-link bioprinted constructions. The structures were created by bioprinting, and GelMA, SilMA, SC-exos, and BMSCs were used as the bioink. (C) Schematic showing that bioprinted constructs can simulate the SC-mediated nerve–bone crosstalk to promote the BMSCs osteogenic function. (D) Schematic showing that bioprinted constructs can improve the bone regeneration microenvironment to promote neurovascularized bone repair.

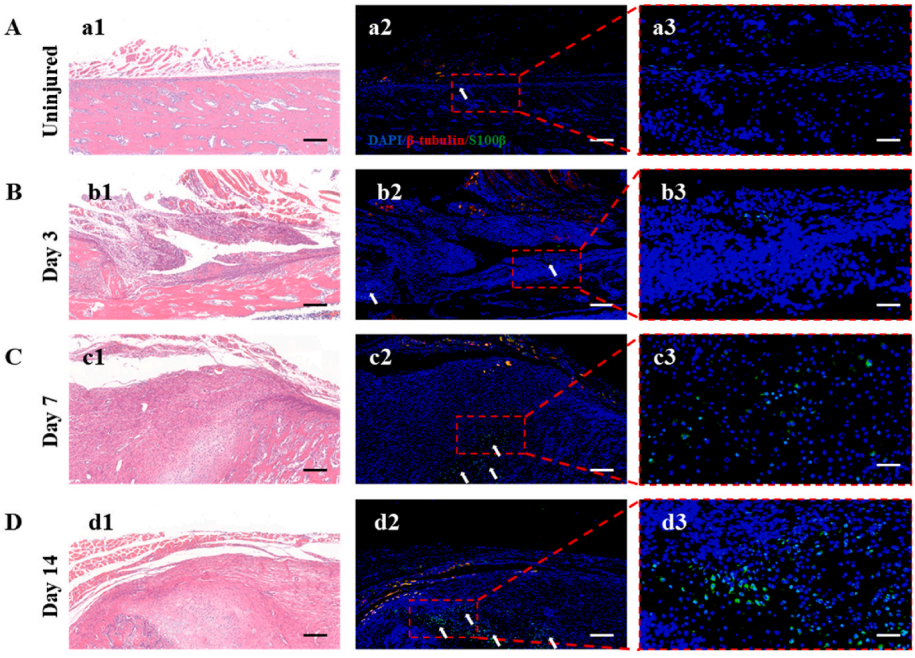

Fig. 2. (A) Expression of β III-tubulin and S100β in bone tissue of rat uninjured femur; (a1) HE staining of the uninjured group; (a2, a3) immunofluorescence staining of β III-tubulin (Red), S100β (green), and DAPI (blue) and corresponding magnified image of the marked area. Scale bar = 1 mm for (a1), (a2); scale bar = 200 μm for (a3). (B–D) Expression of β III-tubulin and S100β in bone tissue of rat injured femur at 3, 7, and 14 d post-fracture; (b1, c1, d1) HE staining of the injured group; (b2, b3, c2, c3, d2, d3) immunofluorescence staining of β III-tubulin (Red), S100β (green), and DAPI (blue) and corresponding magnified image of the marked area. White asterisks denote S100β-positive cells. Scale bar = 1 mm for (b1),(b2),(c1),(c2),(d1),(d2); scale bar = 200 μm for (b3),(c3),(d3).

wounded site of periodontal bone tissue at 7 d post-surgery. In addition, S100β-immunoreactive cells gradually increased from day 14 to day 28 after surgery [3]. This is consistent with our results. Furthermore, Jones et al. demonstrated that SCs primarily regulated bone repair by influencing the biological behavior of stem cells. They found that impaired repair of the mandibular bone after degeneration of the inferior alveolar nerve was related to the proliferative and osteogenic impairment of skeletal stem cells after lacking stimulation of SC paracrine signaling [16]. These studies solidly prove that SCs play a critical role in the microenvironment of bone regeneration, in which the regulation of SCs for stem cells is a crucial pathway for nerve–bone crosstalk.

2.2. Exosomes are an important paracrine pathway for SCs to regulate BMSCs

The osteogenic function of stem cells during bone repair depends on the regulation of niche cells in the microenvironment [6]. The proliferation and osteogenic differentiation of stem cells are crucial for bone regeneration. SCs are important niche cells that have been proven to influence bone regeneration by regulating the osteogenic functionality of stem cells via paracrine signaling [15,16]. Therefore, to investigate whether SCs could regulate the proliferation and osteogenic differentiation of BMSCs through the paracrine pathway, the supernatant of SCs was collected and mixed with α-minimum essential medium (MEM) at specific ratios (10%, 30%, and 50% of SCs supernatant) to form

conditioned medium (CM) for culturing BMSCs, and the normal medium was used as the control group. The osteogenic functionality of BMSCs was assessed by monitoring BMSC proliferation and osteogenic differentiation. The CCK-8 results showed that, compared with the control group, groups cultured in the CM exhibited significantly enhanced cell viability at the 3 and 5 d (Fig. 3A). The effect of the SC paracrine action on the osteogenic differentiation of BMSCs was examined using quantitative reverse-transcription polymerase chain reaction (qRT-PCR), Western blot, and immunofluorescence staining of the osteogenesis-related markers after 7 d of culture. The groups treated with the CM showed a stronger promotion effect on BMSC osteogenic differentiation than that of the control group (Fig. 3B and Fig. S2). These results indicated that SCs could enhance BMSC proliferation and osteogenic differentiation through paracrine signaling.

Exosomes are important paracrine mediators secreted by cells in the microenvironment that play a significant role in intercellular communication [18,45]. To further investigate whether SC-exos are crucial in promoting the proliferation and osteogenic differentiation of BMSCs by SCs, we added the exosome inhibitor GW4869 to block the secretion of exosomes and then collected the cell supernatant. The collected supernatant was mixed with α-minimum essential medium (α-MEM) medium as the new CM, named CM + GW, for BMSC culture. The results of CCK-8, qRT-PCR, Western blot, and immunofluorescence staining in Fig. 3C and D, and Fig. S3 showed that GW4869 impeded the promotion effect of the SC-derived supernatant on BMSC proliferation and osteogenic differentiation. These results suggested that exosomes were crucial in paracrine signaling for SCs to promote the proliferation and differentiation of BMSCs.

2.3. SC-exos encourage BMSC growth and osteogenic differentiation

As critical mediators of intercellular communication, exosomes play

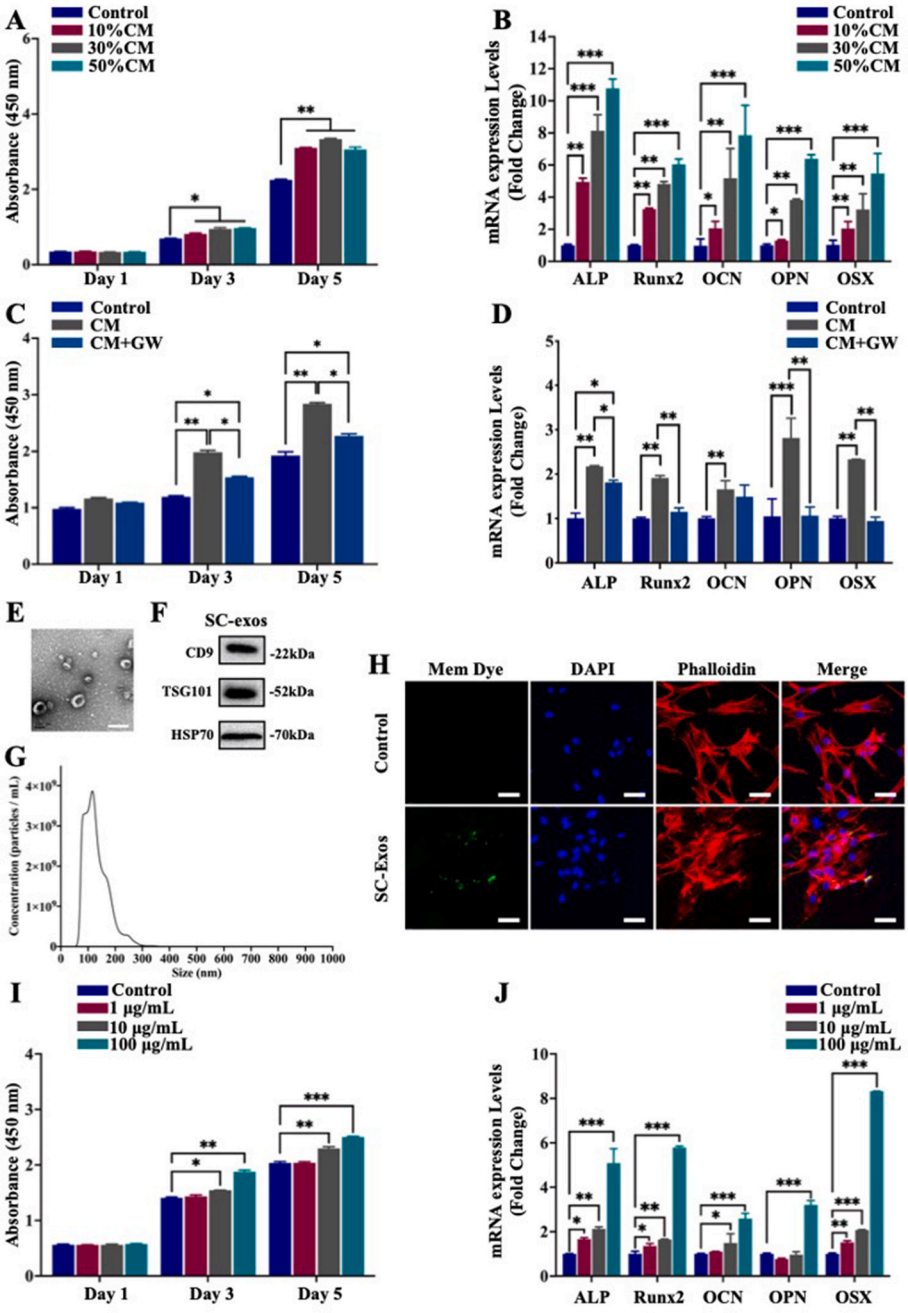

Fig. 3. (A, B) Effects of SC paracrine signaling on BMSCs; (A) cell viability of BMSCs assessed by CCK-8 at 1, 3, and 5 d; (B) qRT-PCR examination of the relative levels of mRNA expression of genes associated with osteogenic development in BMSCs. (C, D) Effect of SC paracrine signaling after pretreatment with GW4869 on BMSCs; (C) cell viability of BMSCs assessed by CCK-8 at 1, 3, and 5 d; (D) qRT-PCR examination of the relative levels of mRNA expression of genes associated with osteogenic development in BMSCs. (E–G) Identification of SC-exos by TEM, NTA, and Western blot for CD9, TSG101, and HSP70. Scale bar = 200 nm. (H) Internalization of SC-exos by BMSCs after 8 h of incubation, as assessed by fluorescence. Green, blue, and red signals represented SC-exos, nucleus, and phalloidin, respectively. Scale bar = 50 μm. (I, J) Effect of SC-exos on BMSCs; (I) cell viability of BMSCs assessed by CCK-8 at 1, 3, and 5 d; (J) qRT-PCR examination of the relative levels of mRNA expression of genes associated with osteogenic development in BMSCs. (*$p < 0.05$, **$p < 0.01$, ***$p < 0.001$).

a crucial role in paracrine communication between SCs and BMSCs. Therefore, the effects of SC-exos on BMSCs were further investigated. SC-exos were isolated and purified from the SC supernatants, and then their morphology, size, and surface protein markers were characterized. As shown in Fig. 3E, the result of transmission electron microscopy (TEM) showed that SC-exos possessed a homogeneous morphology and round vesicle shape with a mean diameter of 130.8 nm ± 1.2 nm. Additionally, the size distribution of SC-exos was determined by nanoparticle tracking analysis (NTA). As shown in Fig. 3G, the majority of the exosomes were in the 30–200 nm size range (92.7%), and the original concentration of SC-exos was 3.20×10^{11} particles mL^{-1}. Western blot was used to assess the expression of the exosomal surface markers CD9, HSP70, and TSG101. As shown in Fig. 3F, CD9, HSP70, and TSG101 were all expressed in SC-exos, thereby confirming the successful isolation of SC-exos.

Exosomes must enter the cytoplasm of recipient cells before performing their function [20]. Exosomes or phosphate-buffered saline (PBS) was labeled with Exosparker (green) and then treated with BMSCs for 0, 4, and 8 h, respectively; thereafter, fluorescence was monitored to indicate exosomal endocytosis. As seen in Fig. 3H, the control group (PBS) did not exhibit green fluorescence, whereas the exosome group did after co-culturing for 8 h. Images observed at different time points and corresponding quantity analysis were exhibited in Fig. S5. The results showed that BMSCs had internalized some SC-exos at 4 h, and more SC-exos were further internalized by BMSCs at 8 h (Fig. S4). These findings suggested that SC-exos could be successfully internalized by BMSCs.

To further confirm whether SC-exos were able to exert the same effect as SCs on BMSCs, we co-cultured BMSCs with SC-exos at doses of 1, 10, and 100 g mL^{-1} as the experimental groups or with PBS as the control group. The results of CCK-8 testing indicated that, for the effect of SC-exos on the proliferation of BMSCs, the 1 μg mL^{-1} group exhibited no significant change compared with the control group; however, a higher concentration of 10 μg mL^{-1} significantly promoted the proliferation of BMSCs. At the concentration of 100 μg mL^{-1}, the promotion effect of SC-exos on the proliferation of BMSCs was further enhanced (Fig. 3I). The qRT-PCR results demonstrated that SC-exos dramatically increased the expression of genes associated with osteogenesis in BMSCs, including ALP, Runx2, OCN, OPN, and OSX (Fig. 3J), with the promotion effect being gradually enhanced by the increase in the added concentration of SC-exos. The results of Western blot results (Fig. S5), alkaline phosphatase (ALP) staining, and Alizarin Red S staining (Fig. S6) also showed that SC-exos promoted the osteogenic differentiation of BMSCs. According to these findings, SC-exos encouraged BMSC proliferation and osteogenic differentiation. Therefore, SC-exos were critical mediators for SCs in the microenvironment to regulate BMSC enactment of bone repair, which could be used to simulate SC-mediated nerve–bone crosstalk.

2.4. The molecular mechanism of exosomal miRNAs of SC-exos on promoting BMSC osteogenic differentiation

Functional miRNAs may be specifically loaded into exosomes and play a significant role in exosome-mediated intercellular

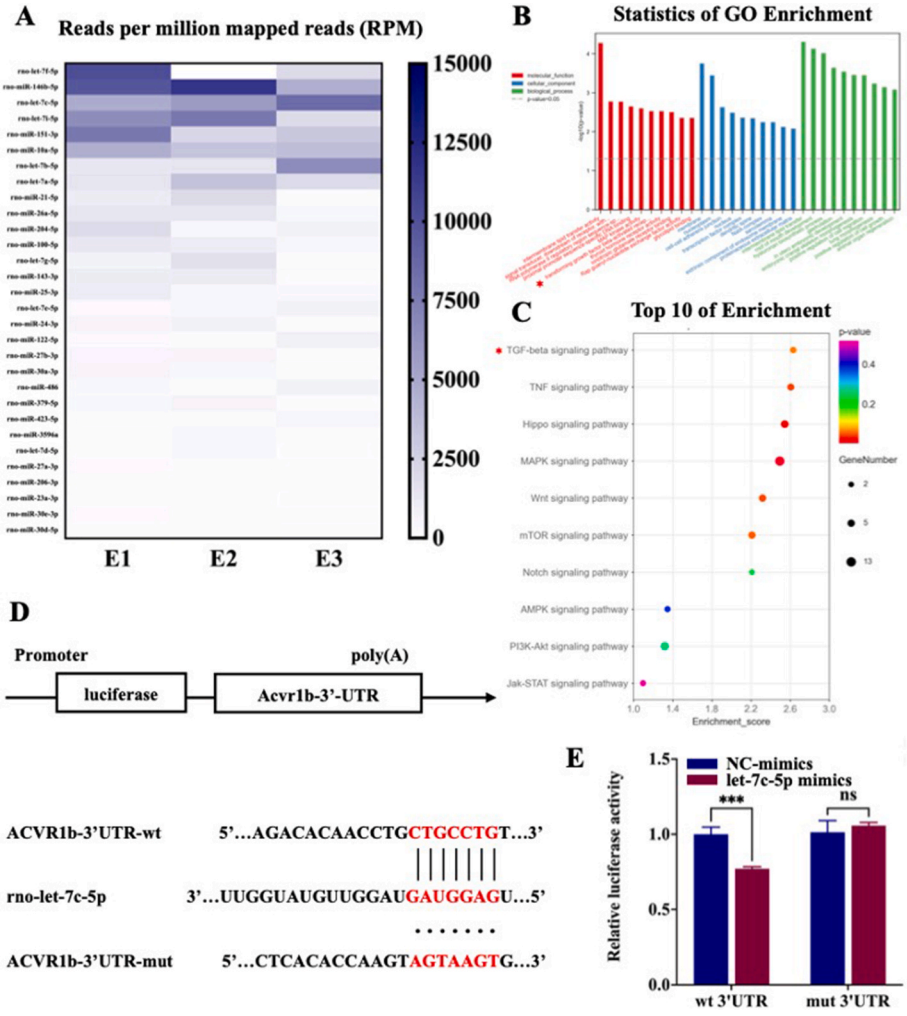

Fig. 4. Small RNA-seq, GO/KEGG analysis, and verification of the let-7c-5p target. (A) A heatmap showing the average readings per million reads (RPM) over the three replicates. The number of miRNAs in SC-exos was determined, and readings with miRNA annotations were normalized to RPM. Present are the top 30 miRNAs that are expressed. (B) GO analyses include functional pathways, biological processes, and cellular components. (C) KEGG pathway enrichment. (D) Acvr1b′s three-prime untranslated region (3′-UTR) predicted target locations. The target area and miRNA were anticipated to couple together, as indicated by red letters. (E) The dual-luciferase reporter assay was used to detect luciferase activity after transfecting 293 T cells with the WT or MUT 3′-UTR of Acvr1b and let-7c-5p. (***$p < 0.001$).

communication [46]. The transfer of exosomal miRNAs to recipient cells for regulating cell behavior is an important mechanism for the biological functions of exosomes [47]. To better understand the underlying mechanism by which SC-exos promoted the osteogenic differentiation of BMSCs, we performed small RNA sequencing (small RNA-seq) of SCs and SC-exos and used Gene Ontology (GO) and Kyoto Encyclopedia of Genes and Genomes (KEGG) analyses of the top 30 expressed miRNAs in exosomes to determine the function of target genes. As seen from the sequencing, the relative contents of different miRNAs in SCs and SC-exos were different, thus proving that the miRNAs were selectively loaded in SC-exos (Fig. S7). Fig. 4A listed the top 30 expressed miRNAs. According to previous reference reports, many miRNAs in the list participated in the biological process related to osteogenic differentiation, and the details were listed in Table S1. Based on previous reports and predicted results of target genes, we further transfected highly enriched miRNAs whose target genes were associated with osteogenic promotion to explore their effects on the osteogenic differentiation of BMSCs. The results showed that let-7c-5p could effectively promote the osteogenic differentiation of BMSCs (Fig. S8).

Furthermore, the target genes of the enriched miRNAs of SC-exos were analyzed using the GO and KEGG databases. GO analysis of target genes revealed that the top 10 participants in molecular functions included TGFβ-activated receptors and that the top 10 of biological processes included positive regulation of cell migration and positive regulation of cell growth (Fig. 4B). In addition, Fig. S7 showed the specifics of small RNA-seq and the analysis of three directed acyclic graphs regarding the top 10 activities for biological processes, molecular functions, and cellular components. KEGG pathway analysis revealed the top 10 of osteogenesis-related pathways after screening; as shown in Fig. 4C, the TGFβ signaling pathway might be the most critical pathway for SC-exos to promote osteogenic differentiation. After further analysis and prediction, let-7c-5p, which was highly enriched in SC-exos, had the potential to regulate the TGFβ signaling pathway by targeting Acvr1b for promoting the osteogenic differentiation of BMSCs.

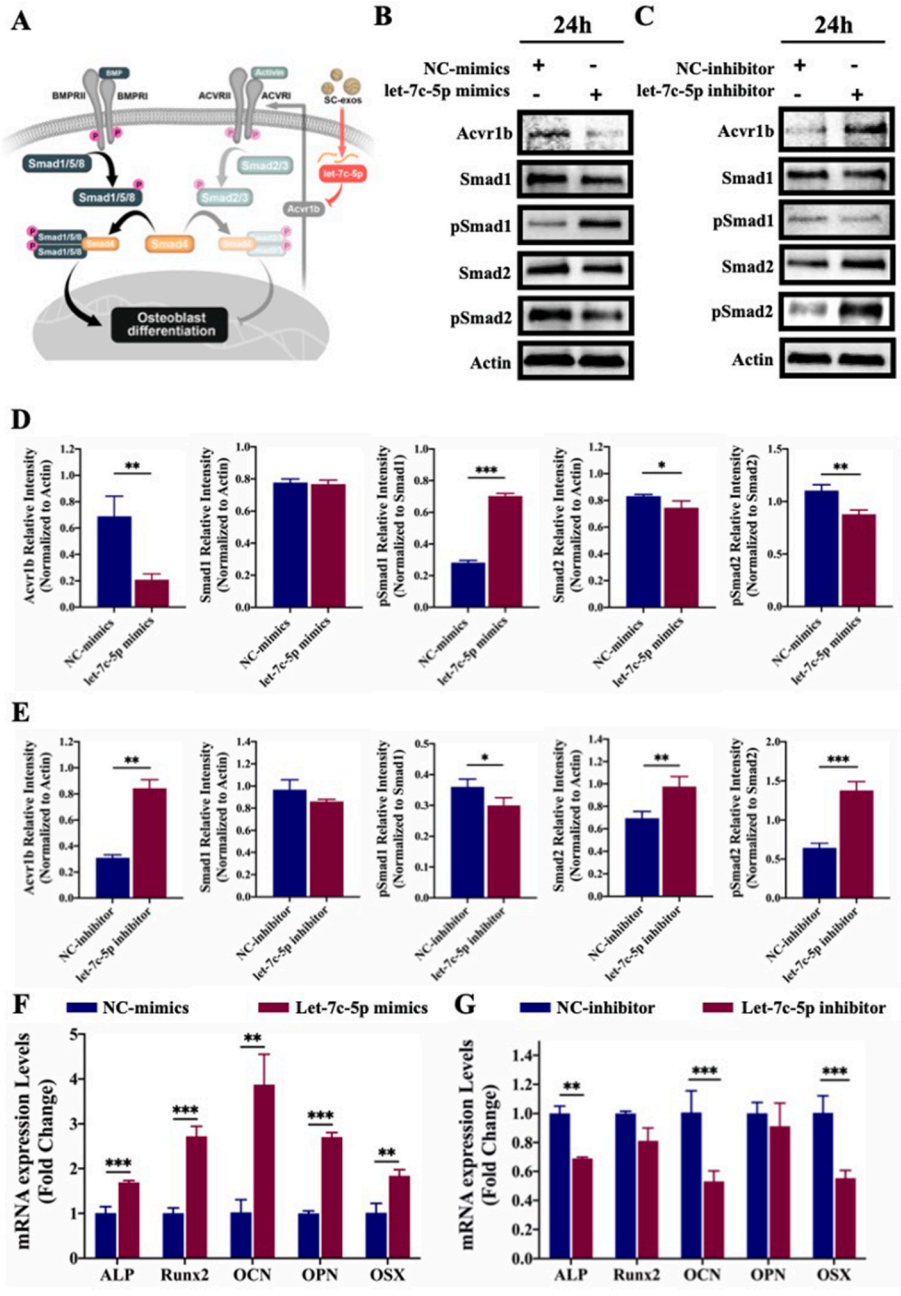

Fig. 5. (A) Schematic showing that let-7c-5p regulates the competitive balance between activin-elicited Smad2/3 and BMP-elicited Smad1/5/8 by targeting Acvr1b gene. (B–E) Expression of Acvr1b, Smad (Smad1, Smad2), and phosphorylated Smad (pSmad1, pSmad2) proteins in BMSCs analyzed by Western blot and its corresponding densitometric semiquantitation after transfection with let-7c-5p mimics or inhibitor. (F, G) The qRT-PCR analysis regarding the effect of transfection with let-7c-5p mimics or inhibitor on the osteogenic differentiation of BMSCs. (*$p < 0.05$, **$p < 0.01$, ***$p < 0.001$).

Transforming growth factor (TGF), bone morphogenic proteins (BMPs), and activin/inhibin are all included in the TGF-β family of cytokines, which is crucial in the regulation of osteoblast differentiation and bone formation [48–50]. The BMP signaling pathway is activated by ligands of the bone morphogenetic protein family, such as BMP-2, which is essential for bone formation and homeostasis. BMP-2 can bind to the extracellular domain of the type II receptor (BMP receptor 2 [BMPR2]), which subsequently phosphorylates the type I receptor (BMP receptor 1 [BMPR1]). Activated BMPR1-type receptors initiate intracellular signaling by phosphorylating specific Smad proteins, namely, Smad1/5/8. Phosphorylated Smad1/5/8 and Smad4 form a complex, which subsequently translocates to the nucleus to participate in transcriptional reactions. This promotes the expression of important transcription factors and transcriptional co-activators in cells and, consequently, BMSC osteogenic differentiation [51]. Activin signals via the type I receptors (Activin receptor [Acvr]1b and 1c) can initiate intracellular signaling by phosphorylating the specific Smad proteins-Smad2/3, with the phosphorylated Smad2/3 protein also forming a complex with Smad4 and playing an opposite role to Smad1/5/8 [52]. Therefore, the potential competition between Smad1/5/8 and Smad2/3 for Smad4 is considered to be a potent regulator of the canonical Smad pathway [53]. According to the results of our miRNA sequencing and the prediction of target genes, we speculated that let-7c-5p could inhibit the activation of activin-elicited Smad2/3 by targeting the Acvr1b gene, thus promoting the activation of BMP-elicited Smad1/5/8 and, consequently, the osteogenic differentiation of BMSCs (Fig. 5A).

The bioinformatics analysis results in Fig. 4D displayed the expected binding locations for let-7c-5p and Acvr1b. To further confirm our prediction, the dual-luciferase reporter assay was used to determine whether let-7c-5p directly targeted the Acvr1b gene. The luciferase activity in the let-7c-5p and Acvr1b-wt co-transfection group was significantly lower than that in the other groups ($p < 0.001$), indicating that Acvr1b was a direct target of let-7c-5p (Fig. 4E). To further verify the regulation of let-7c-5p on activin-elicited Smad2/3 and the corresponding influence of BMP-elicited Smad1/5/8, let-7c-5p mimics or inhibitor were transfected into BMSCs, and the expression of Acvr1b, Smad, and phosphorylated Smad proteins (Smad1, pSmad1, Smad2, and pSmad2) were then detected by Western blot. The results of poly(A)-tailed qRT-PCR showed that let-7c-5p was substantially elevated following transfection with let-7c-5p mimics, with let-7c-5p only being marginally downregulated after transfection with the let-7c-5p inhibitor (Fig. S9). This outcome may be attributed to the low basic level of let-7c-5p in BMSCs. Furthermore, qRT-PCR was used to identify the expression of the Acvr1b gene following transfection with let-7c-5p mimics or inhibitors. The results showed that let-7c-5p could inhibit the expression of the Acvr1b gene (Fig. S9). The results of the Western blot showed that let-7c-5p mimics significantly downregulated the expression of Acvr1b protein, thus upregulating the expression of pSmad1 and suppressing the expression of pSmad2 (Fig. 5B). After transfection with the let-7c-5p inhibitor, the opposite results were obtained (Fig. 5C), suggesting that let-7c-5p could inhibit the activation of activin-elicited Smad2/3 by targeting the Acvr1b gene, thus promoting the activation of BMP-elicited Smad1/5/8. To determine the role of let-7c-5p in the osteogenic differentiation of BMSCs, we used let-7c-5p mimics or inhibitor to transfect BMSCs and analyzed the expression of osteogenesis-related genes (ALP, Runx2, OCN, OPN, and OSX). According to qRT-PCR results, the bone formation-related genes ALP, Runx2, OCN, OPN, and OSX were significantly upregulated in the let-7c-5p mimics group compared with their expression in the control group (Fig. 5F). The let-7c-5p inhibitor prevented the osteogenic differentiation of BMSCs (Fig. 5G). To further verify the osteogenic differentiation of BMSCs, the immunofluorescence staining of Runx-2 and OPN was performed. As shown in Fig. S10, let-7c-5p mimics could significantly promote the expression of Runx-2 and OPN, whereas let-7c-5p inhibitor inhibited the expression of Runx-2 and OPN. These findings suggested that let-7c-5p could encourage the osteogenic differentiation of BMSCs; therefore, the abundant let-7c-5p of SC-exos facilitated the osteogenic differentiation of BMSCs by targeting Acvr1b gene to prevent the activation of activin-elicited Smad2/3.

2.5. Bioinks are designed, prepared, and characterized

GelMA and SilMA, which are synthesized from gelatin and silk, respectively, by a simple reaction with methacrylic anhydride have been widely used as bioinks for co-culture with cells [54]. Through the photoactivation of the vinyl groups, GelMA and SilMA can be covalently bonded to create an elastic hydrophilic polymer network that is stable and conducive to cell culture. GelMA is often selected as the substrate component of bioink because of its good temperature-sensitive properties, biocompatibility, and printability. SilMA has been widely used in bone tissue engineering because of its tunable mechanical strength and flexibility, biocompatibility, and osseointegration [34]. Moreover, SilMA can be used as an ideal carrier for enzymes, biological factors, antibiotics, and exosomes, extending their release period [36]. Therefore, to optimize the release process of exosomes, we used a hybrid bioink system composed of GelMA and SilMA in this study. Considering the printability and the ability of bioink to sustain release exosomes, in combination with previous reports, we mixed GelMA and SilMA in three ratios to produce the following three bioinks: 10% GelMA (containing 10 w/v% GelMA), 8/2% GelMA/SilMA (containing 8 w/v% GelMA and 2 w/v% SilMA), and 6/4% GelMA/SilMA (containing 6 w/v% GelMA and 4 w/v% SilMA). The release kinetics of the exosomes were evaluated. After loading the exosomes with 10% GelMA, the cumulative release of exosomes exceeded 90% of the total amount of loading on day 9. After the addition of SilMA, the release rate of exosomes significantly slowed, and the exosome release period was extended for as long as 24 d for the 6/4% GelMA/SilMA bioink (Fig. 6A). This outcome indicated that the addition of SilMA decreased the release rate of exosomes, which were released in a more sustainable manner. Next, the rheological properties of the bioinks were investigated. As shown in Fig. 6B and C, the temperature of sol–gel transformation of the bioinks increased, and the viscosity of the bioinks decreased with the decrease in GelMA and increase in SilMA in the bioink. These results indicated that the addition of SilMA affected the low-temperature preprinting performance of materials, which was crucial in the bioprinting process. After comprehensive consideration, we selected the 8/2% GelMA/SilMA as the bioink for subsequent studies. Scanning electron microscopy (SEM) was used to examine the microstructures of the hydrogels. The bioink with macropores, seen in Fig. 6D, was suitable for cell migration, proliferation, and tissue healing.

2.6. Bone repair constructs are produced by 3D bioprinting

Using a temperature-controlled air extrusion-based 3D bio-printer, bioprinted constructs were quickly prepared based on the rheological characteristics of the bioink. Before bioprinting, SC-exos (100 μg mL^{-1}) and BMSCs (10^7 cells mL^{-1}) were introduced to the bioink. These bioprinted constructs were called the SC-exos@G/S group, and the bioprinted constructs without SC-exos were the G/S group. To guarantee that the bioink was not sticky and to lessen the impact of shear strain on cells during extrusion, the bioink was fed into the printing cartridges at 25 °C. The temperature of the print nozzle and platform was maintained at 15 °C to enable the deposition of a stable, smooth filament and the stability of the printed construct throughout printing. After the printed constructs were exposed to ultraviolet light to cause photocrosslinking, the final structures of the constructs were produced. The morphology of a sample printed hydrogel construct with consistently spaced ordered macropores was shown in Fig. 6E.

Next, the biocompatibility of the bioprinted constructs was evaluated. Live/dead staining results showed high cell viability reaching 95% in the bioprinted constructs at 3d after printing (Fig. 6F). To detect the

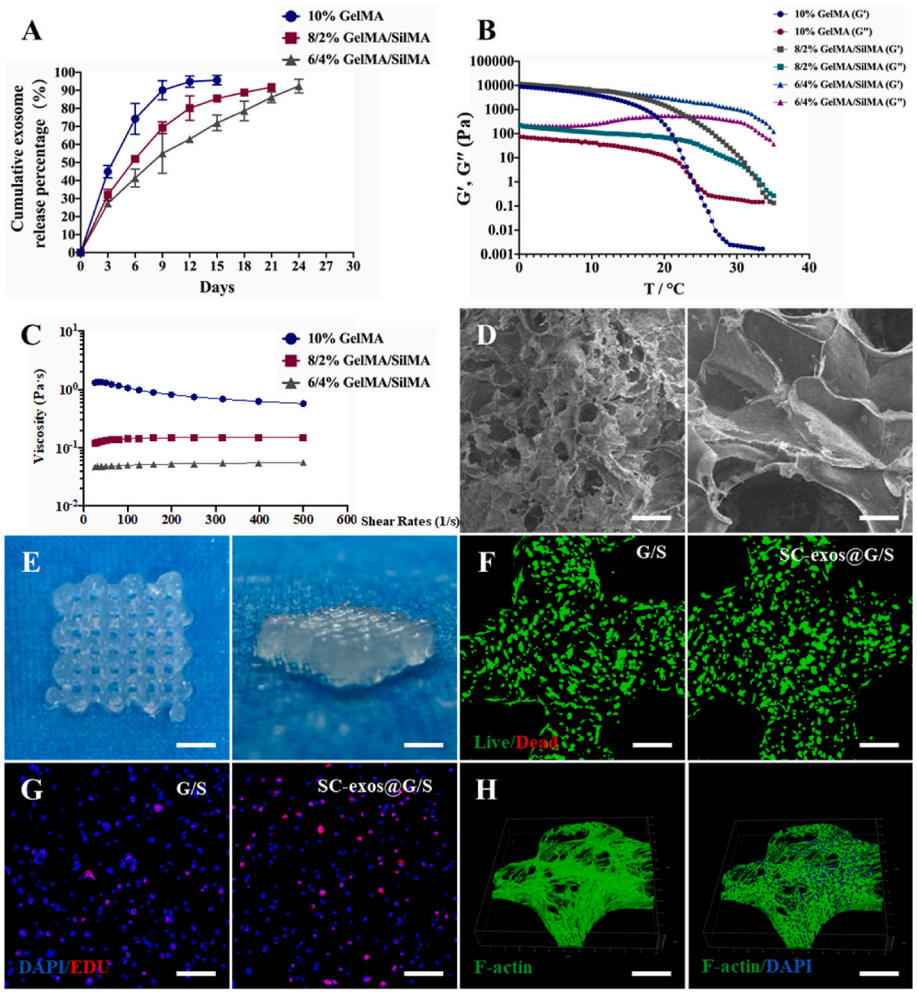

Fig. 6. (A) Release curve of exosomes from the different ratio of bioinks. (B) G′ and G″ of bioinks with different ratios. (C) Stress-strain curves of bioinks with different ratios. (D) Scanning electron micrographs of a bioink composed of 8% GelMA and 2% SilMA, scale bar = 100 μm (left) or scale bar = 25 μm (right). (E) Photograph of bioprinted microfibrous constructs with different thicknesses, scale bar = 500 μm. (F) The biocompatibility of bioprinted constructs was assessed by live/dead staining after cultured for 3 d, scale bar = 200 μm. (G) Evaluation of the proliferation of loaded BMSCs in constructs via EdU staining, scale bar = 200 μm. (H) Cytoskeleton staining of BMSCs in bioprinted constructs with a bioink composed of 8% GelMA and 2% SilMA, scale bar = 200 μm.

effect of the bioprinting process on cell activity, the live/dead staining assay of bioprinted constructs was performed at 4 and 24 h after bioprinting. As shown in Fig. S11, few dead cells were visible in the bioprinted constructs, indicating high cell viability in the bioprinted constructs at 4 and 24 h after printing. These results demonstrated that cells were only slightly damaged during printing. The 5-Ethynyl-2′-deoxyuridine (EdU) staining was used to determine the proportion of proliferating cells in the bioprinted constructs. The results showed that the proportion of proliferating cells in the SC-exos@G/S group was higher than that in the G/S group, indicating that the addition of SC-exos promoted the proliferation of BMSCs in constructs (Fig. 6G). Furthermore, after culturing for 7 d, the number of cells in the bioprinted constructs continued to increase (Fig. S12). Additionally, following 14 d of culture, 4′,6-diamidino-2-phenylindole (DAPI) staining of the BMSCs nuclei and F-actin staining of the cytoskeleton revealed that the cells had almost entirely covered the scaffold structure; these results indicated that the bioprinted constructs were beneficial to the proliferation and migration of cells (Fig. 6H) and confirmed the excellent cytocompatibility of the bioprinted constructs.

2.7. Bioprinted constructs can simulate the SC-mediated nerve–bone crosstalk

After being loaded with BMSCs in all groups, the constructs were grown in the medium for 7 d before the osteogenesis-related genes were examined to assess the osteogenic differentiation of BMSCs in vitro. The osteogenic development of BMSCs in the bioprinted structures in vitro was evaluated using immunofluorescence labeling (Fig. 7A and B) and qRT-PCR (Fig. 7C). The results showed that BMSCs in the SC-exos@G/S group possess higher osteogenic activity than those of the G/S group. The findings supported the hypothesis that SC-exos@G/S constructs could successfully simulate the intercellular communication between SCs and BMSCs and promoted the BMSC osteogenic differentiation in vitro.

In this study, a subcutaneous implant model was employed to evaluate the potential of bioprinted structures for osteogenic differentiation in vivo (Fig. 7E). The bioprinted constructs were collected at 14 d post-implantation for immunofluorescence labeling and qRT-PCR, and the outcomes were in line with those seen in vivo. The SC-exos@G/S group had a more significant expression level of osteogenesis-related genes than the G/S group (Fig. 7D). Compared to that in the G/S group, the expression of the osteogenic differentiation marker was considerably higher in the SC-exos@G/S group (Fig. 7F). These findings demonstrated that the SC-exos@G/S construct simulated the regulatory function of SCs on BMSCs to achieve increased osteogenic activity in vivo.

2.8. Bioprinted constructs can improve the bone regeneration microenvironment to promote innervation and vascularization

In the bone repair process, the regeneration of nerves and blood vessels is crucial for effective bone healing. Therefore, the ability of the SC-exos@G/S constructs to promote innervation and vascularization was assessed using a subcutaneous implantation model in Sprague–Dawley (SD) rats and the G/S constructs were used for comparison. The constructs were collected for further analysis at 14 d post-implantation.

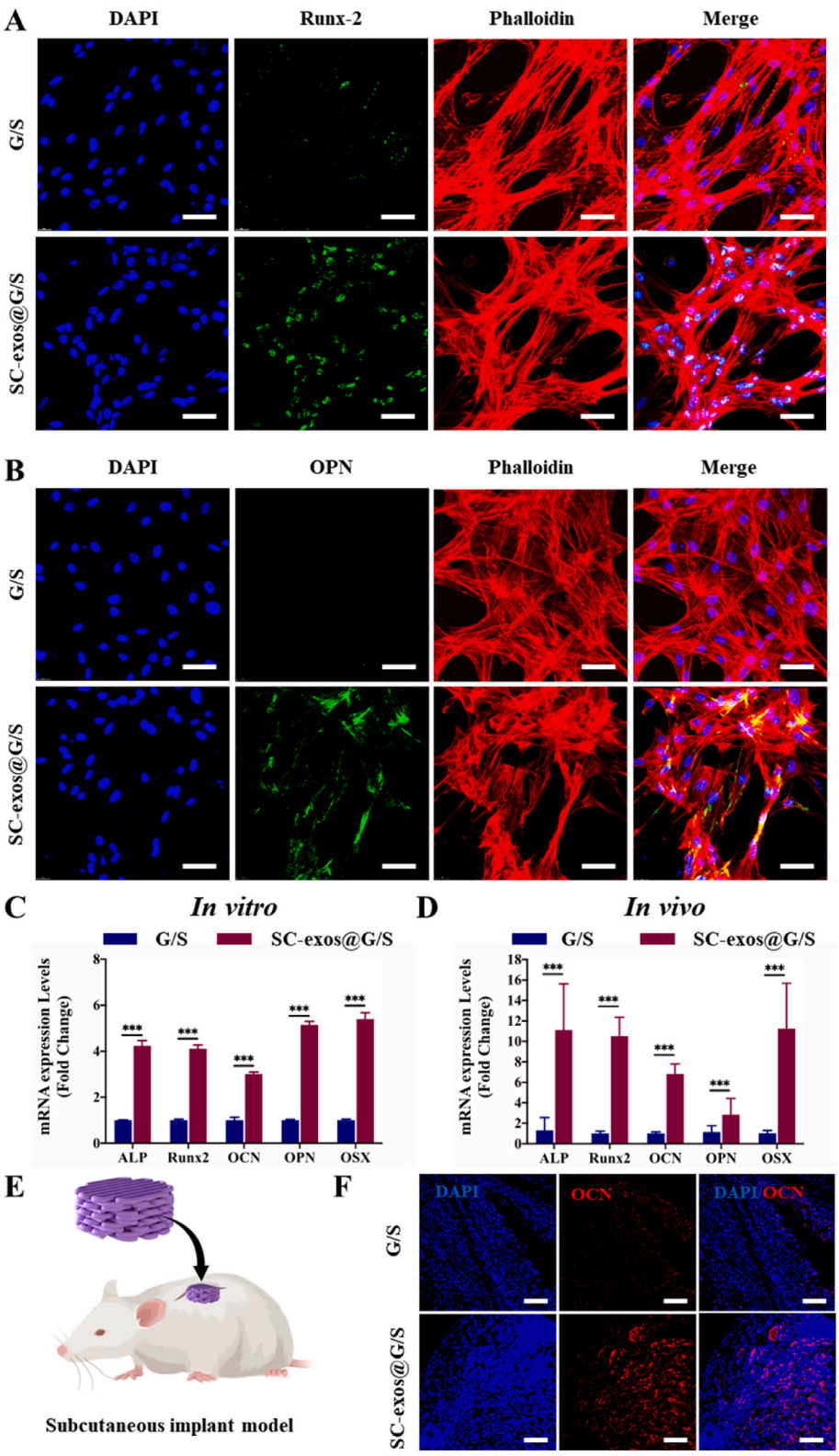

Fig. 7. The osteogenic function of bioprinted constructs in vitro and in vivo. (A) Immunofluorescence staining for Runx-2 in bioprinted constructs after culture for 7 d in vitro, scale bar = 50 μm. (B) Immunofluorescence staining for OPN in bioprinted constructs after culture for 7 d in vitro, scale bar = 50 μm. (C) qRT-PCR examination of the relative levels of mRNA expression of genes associated with osteogenic development in bioprinted constructs in vitro. (D) qRT-PCR examination of the relative levels of mRNA expression of genes associated with osteogenic development in bioprinted constructs after implantation for 14 days. (E) Schematic showing the preparation of the subcutaneous model. (F) Expression of osteogenic specific gene OCN in bioprinted constructs was detected by immunofluorescence staining after implantation for 14 d, scale bar = 100 μm. (*$p < 0.05$, **$p < 0.01$, ***$p < 0.001$).

To assess the innervation potential of the bioprinted constructs, immunofluorescence staining of NF200 and MBP was performed in all groups. Numerous immunofluorescence signals were observed in the SC-exos@G/S group, indicating that the SC-exos@G/S constructs were well-innervated, whereas the immunofluorescence signals were hardly observed in the G/S group (Fig. 8A). These results indicated that SC-exos@G/S constructs could induce innervation by releasing SC-exos in vivo.

Before the animals were sacrificed, blood perfusion in the constructions was measured using ultrasound imaging to determine the degree of vascularization. In the SC-exos@G/S group, a robust blood flow signal was observed at 7 d, indicating sufficient blood supply inside the constructs. In comparison, the G/S group hardly showed any blood flow indication (Fig. 8C). Day 14 post-implantation, the blood flow

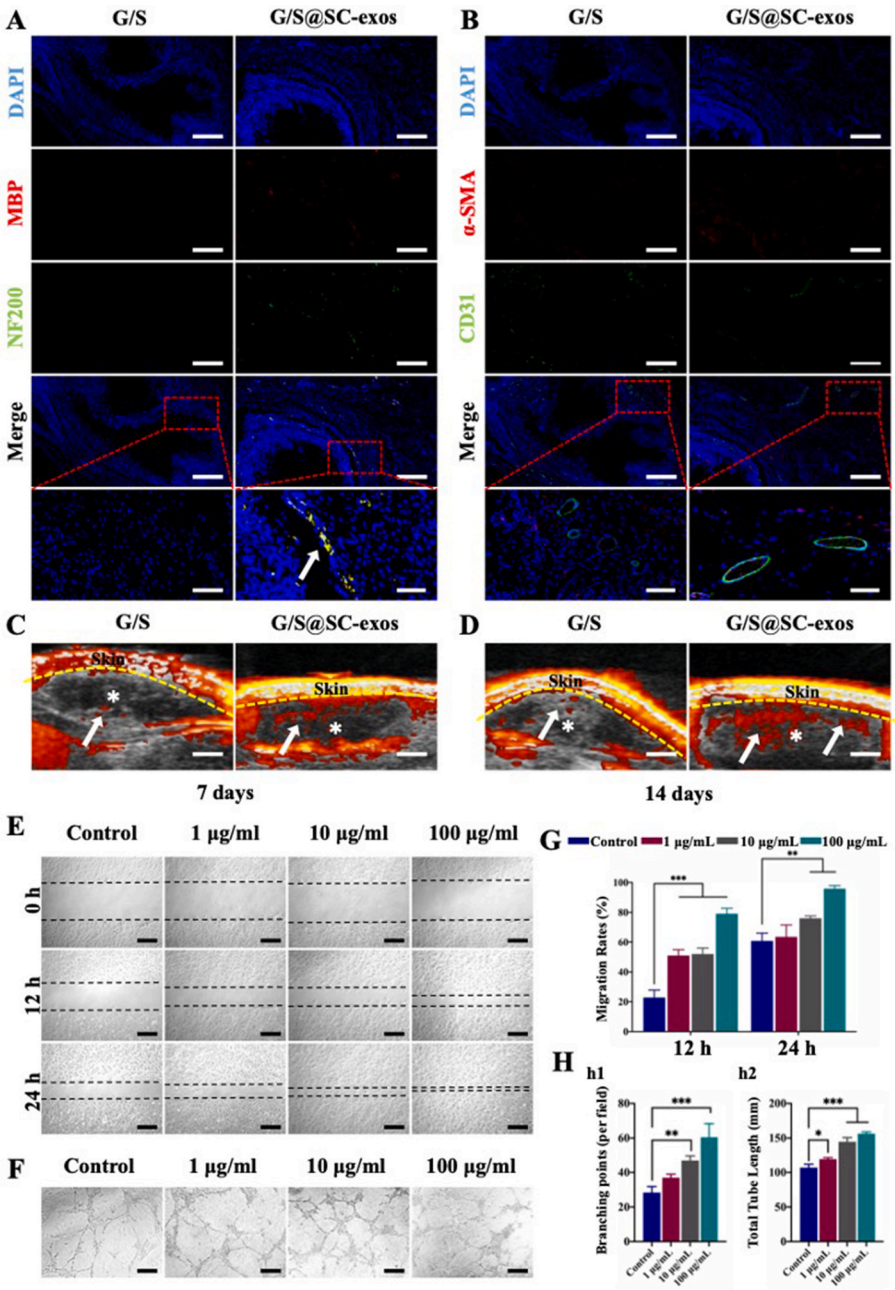

Fig. 8. (A) Histological analysis of subcutaneous implantation constructs for nervous structures. Blue, red, and green signals represent the nucleus, MBP, and NF200, respectively. Scale bar = 200 or 50 μm. (B) Histological analysis of subcutaneous implantation constructs for vascular structures. The blue, red, and green signals represent the nucleus, α-SMA, and CD31, respectively. Scale bar = 200 or 50 μm. (C, D) After 7 and 14 d of implantation, ultrasound images of implanted structures were obtained. White asterisks and arrowheads denote the hydrogel and vascular systems, respectively. Scale bar = 2 mm. (E) Scratch wound assay of EPCs. Scale bar = 200 μm. (F) Tube formation assay of EPCs. Scale bar = 100 μm. (G) Analysis of the migration assay. (H) Quantitative analysis of (h1) branching points and (h2) total tube length. (*$p < 0.05$, **$p < 0.01$, ***$p < 0.001$).

signal in the SC-exos@G/S group was further improved, whereas the blood flow signal in the G/S group was still hardly detectable (Fig. 8D). The vascular structures in the constructs and surrounding tissue were further assessed using immunofluorescence labeling for α-SMA and CD31. In Fig. 8B, several vascular structures were seen in the SC-exos@G/S group, whereas only a few were visible in the G/S group. These results indicated that SC-exos@G/S constructs had an excellent capability for angiogenesis in vivo, revealing that SC-exos potentially promoted vascularization in the microenvironment. Therefore, the scratch assay and tube formation assay were performed to test whether SC-exos could promote angiogenesis directly. As shown in Fig. 8E and F, SC-exos promoted the migration and enhanced the tube formation performance of endothelial progenitor cells (EPCs), which indicated that SC-exos effectively promoted the angiogenesis of EPCs.

2.9. SC-exos@G/S are evaluated to improve bone regeneration effect in vivo

Finally, a rat cranial defect model was used to examine the impact of bioprinted constructions on bone healing. The radiographic results of bone development were exhibited in Fig. 9A. The SC-exos@G/S group showed the best bone formation promotion impact, with new bone tissue almost completely filling the defect location followed by the G/S group. Only a few new bones formed in the Exo and control groups, with no discernible difference in the bone repair impact observed between the two groups. Fig. 9B displayed the outcomes of micro-CT quantitative analysis. According to the findings, the SC-exos@G/S group (29.242% ± 7.681%, $p < 0.001$) had a considerably larger bone-to-tissue volume ratio (BV/TV) than those of the G/S (15.977% ± 3.577%, $p < 0.05$) and Exo (8.329% ± 1.826%, $p < 0.05$) groups. The control group had the lowest ratio (6.02575% ± 1.085%, $p < 0.001$). Similar patterns were observed in bone mineral density (BMD) among the other groups.

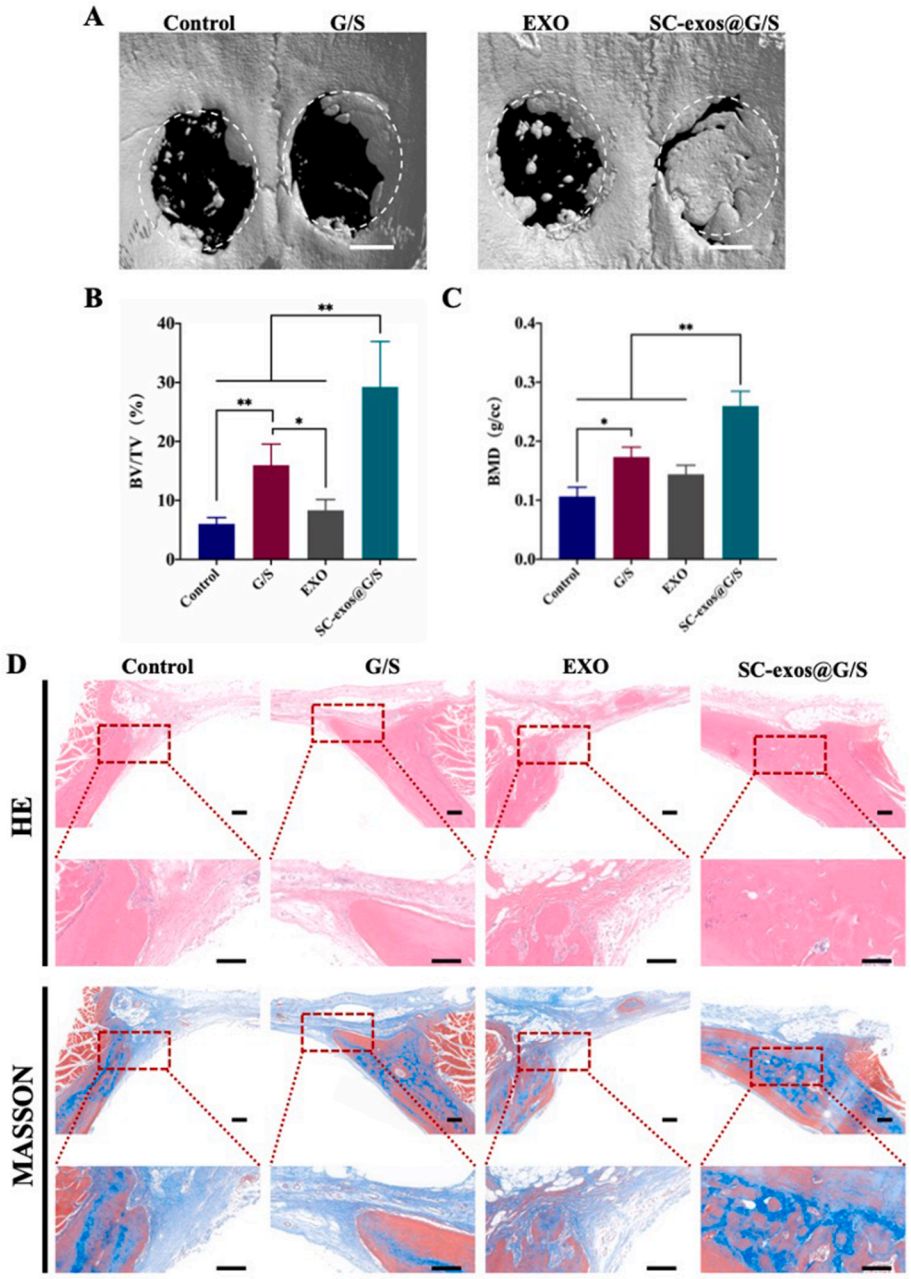

Fig. 9. (A) 3D reconstruction of micro-CT images, scale bar = 2 mm. (B, C) Quantitative analysis of micro-CT images, including BV/TV and BMD. (D) HE and Masson staining of different groups in vivo, scale bar = 100 μm. (n = 6, $*p < 0.05$, $**p < 0.01$).

Additionally, hematoxylin and eosin (HE) and Masson's trichrome staining were carried out at 8 weeks post-surgery. Whole samples are exhibited in Fig. S13, supplementary information. In line with the radiological findings, the specimen analysis results clearly showed that the bone defect in the SC-exos@G/S group was almost entirely repaired, whereas that in the G/S group only had minimal healing success. By contrast, the Exo and control groups showed no healing effect (Fig. 9D). Therefore, the bone repair effect of simple bioprinted constructs or direct one-time in-situ injection of large doses of exosome was limited, whereas SC-exos@G/S constructs could better promote bone repair by simulating the function of SC-exos in the bone regeneration environment.

3. Discussion

Nerves are present throughout the entire bone and are mainly distributed in the periosteum, bone marrow, and mineralization areas [5]. Crosstalk between nerves and bone is involved in bone development, metabolism, and repair [55]. Many humans and animal species have demonstrated the importance of the nervous system regulation for bone repair and that the lack of nerve–bone crosstalk impairs bone repair [9,56–58]. SCs are essential cell components of the peripheral nervous system in the bone regeneration microenvironment and participants in bone repair [14,39]. Our results also demonstrated that in the early stage after bone injury, SCs were present at the injury site and associated callus, which indicated their involvement in the process of bone repair. According to Jones et al. paracrine signaling from SCs was required for skeletal stem cells to enact bone healing in the bone regeneration microenvironment [16]. Therefore, the effects of SCs on BMSCs may be an important pathway for the crosstalk between nerves and bone during bone regeneration. To enhance nervous system regulation in bone repair, improve the bone regeneration microenvironment,

and provide a more effective tissue engineering strategy for bone defect repair, this study aims to investigate the mechanism of SCs to regulate bone repair and develop tissue-engineered constructs that simulate SC-mediated nerve–bone crosstalk.

Exosomes, which are a kind of extracellular vesicle, are produced by all cells and are frequently present in the microenvironment [17,18]. The ability of cells to regulate tissue repair is partly derived from their exosomes [20,36]. Previous research demonstrated that Schwann cell-derived extracellular vesicles (SC-EVs) and the CM formed from SC supernatant encouraged the proliferation and osteogenic differentiation of human dental pulp stem cells [59]. Similar results were found in our study, that is, SC-CM was able to promote BMSC proliferation and osteogenic differentiation. Therefore, the regulatory effects of SCs on BMSCs in the bone regeneration microenvironment are supposedly derived from their paracrine action, to which exosomes may contribute. Furthermore, we used GW4869 to block the secretion of SC-exos and then explored their role in the paracrine action of SCs on BMSCs. The results demonstrated that SC-exos were an important paracrine pathway that mediated the communication between SCs and BMSCs. The results of direct co-culture of SC-exos with BMSCs were also consistent with this conclusion. Furthermore, the molecular mechanism of SC-exos in promoting the osteogenic differentiation of BMSCs was also investigated to further explain the role of SCs in promoting bone repair. The multiple biological functions of exosomes are derived from their abundant miRNAs. Exosomes can deliver certain miRNAs to recipient cells, thereby altering the gene expression and consequently influencing the biological behaviors of recipient cells. Therefore, this study attempted to explore the underlying molecular mechanisms of SC-exos in promoting the osteogenic differentiation of BMSCs by exosomal miRNAs. Based on the results of the small-RNA sequencing and bioinformatic analysis, we found that the TGFβ signaling pathway was crucial for SC-exos to regulate the osteogenic differentiation of BMSCs through miRNAs. BMP and activin are important members of the TGFβ family, which is crucial in osteogenic differentiation [50,52]. BMP can activate Smad1/5/8 phosphorylation, which has a positive regulation effect in bone formation. However, activin depends on the Acvr1b/1c to activate the phosphorylation of Smad2/3, which plays an inhibiting role in bone formation. The abundant let-7c-5p within SC-exos can inhibit the activation of the activin-Smad2/3 signaling pathway by targeting the Acvr1b gene and thus promote the activation of the BMP-Smad1/5/8 and BMSC osteogenic differentiation. In addition, other components of exosomes, such as proteins and other RNAs, are important in exosome function, participating in the communication between the bone and SCs. Proteomic studies of exosomes have received wide attention. Besides being abundant in membrane localization proteins, exosomes also contain other different types of proteins, such as enzymes, hormones, cytokines, ligands, and other proteins, which are involved in their regulation. According to Wang et al. the SC-EVs can promote the migration and osteogenic differentiation of dental mesenchymal stem cells by transferring stromal cell-derived factor 1 [59]. In addition, the different RNA species in exosomes, including mRNA and non-coding RNA, are also reported to regulate the biological functions of recipient cells. In a study by Li et al. RCS96-EVs were able to enhance the expression of several transcription factors (Sox2, Nanog, and Oct4) to promote the proliferation and multipotency of human dental pulp cells by transferring their mRNAs [60]. Therefore, owing to the complexity of the cargo exosomes carry, subsequent studies need to be performed to more comprehensively explore the mechanisms and effects of SC-exo regulation of BMSCs. In addition, Parfejevs et al. found that SCs could activate the TGFβ signaling pathway to promote skin wound healing by increasing paracrine signaling [61]. Similarly, Hao et al. found that the GelMA-loaded SC-exos could promote the osteogenic differentiation of BMSCs by activating the TGF-β/Smad signaling pathway [26]. Therefore, the activation of the TGFβ signaling pathway may be an important mechanism in SC-regulated tissue repair. In summary, SC-exos is an important link in the process of nerve regulation of the bone regeneration microenvironment. Logically, we can partially simulate nerve–bone crosstalk through bioprinted constructs of SC-exos@G/S to improve the bone regeneration microenvironment for neurovascularized bone regeneration.

To simulate the SC-mediated nerve–bone crosstalk, SC-exos and BMSCs were added to the bioink for bioprinted constructs. Although many hydrogels are considered to be ideal carriers for loading exosomes, the rapid release of exosomes impairs their effects. SilMA has been proven as a carrier for optimizing the release process of exosomes such that they can perform their function effectively. Therefore, we used a hybrid hydrogel system composed of GelMA and SilMA mixed in different ratios and tested their printability and sustained release efficiency of exosomes. With the addition of SilMA, the release manner of exosomes from hybrid hydrogels was markedly improved. This result may be due to the release of exosomes being influenced by the degradation properties of the hybrid hydrogel. The addition of SilMA delayed the degradation of the hybrid hydrogels, thus arresting the exosome release rate. However, the addition of SilMA affected the low-temperature preprinting performance of materials. After a comprehensive analysis, the 8/2% GelMA/SilMA showed the optimal sol–gel transformation temperature and excellent exosome release manner; thus, this hydrogel was ultimately selected as the bioink for bioprinting.

The bioprinted SC-exos@G/S constructs exhibited excellent promotion of bone regeneration and neurovascular network growth both in vivo and in vitro. In vitro, abundant of osteogenesis-related markers, that is, OPN and Runx2-expressing cells, were observed in the SC-exos@G/S group; by contrast, these markers were hardly observed in the G/S group. Similarly, in the subcutaneous model, the bioprinted constructs and surrounding tissue had a higher expression of OCN in the SC-exos@G/S group than those in the G/S groups. These results confirmed that the SC-exos@G/S constructs successfully simulated the SC-mediated nerve–bone crosstalk to regulate the osteogenic differentiation of BMSCs in vivo. As repair cells originating from the peripheral nervous system, SCs can promote the regeneration of peripheral nerves. The ability of cells to promote tissue repair is partly due to their exosomes. Lopez-Verrilli et al. indicated that SC-exos could promote neurite extension and axonal regeneration in vitro [22]. In our studies, after 14 d of subcutaneous implantation in vivo, more neural structures were found in the SC-exos@G/S group than those of the G/S group, indicating more innervation in SC-exos@G/S constructs. Moreover, the results of immunofluorescence staining showed that the number of vascular constructs in the SC-exos@G/S group had increased, indicating that the addition of SC-exos promoted angiogenesis. We believe two possible reasons can explain this outcome: first, SC-exos can directly promote angiogenesis in the microenvironment. Our further study indicated that SC-exos promoted the migration and tube formation of the performance of EPCs, which was significant for angiogenesis. Secord, neurons are also able to influence angiogenesis by neuropeptides; consequently, the reconstruction of the nervous system within the SC-exos@G/S constructs also promotes the reconstruction of blood vessels. These results indicated that the SC-exos@G/S constructs could improve the microenvironment by releasing SC-exos to exert the repair effects of SCs, promote innervation and vascularization, and further promote effective bone repair. Finally, the effect of bioprinted constructs in promoting bone defect repair was evaluated in an SD-rat cranial defect model. The SC-exos@G/S group exerted the strongest promotion effect on the formation of new bone in the defect. Although the process by which the nervous system regulates bone repair is complex, we conclude that SCs play an important role in the bone regeneration microenvironment by promoting innervation, vascularization, and osteogenesis through exosomes. Based on these results, simulating SC-mediated nerve–bone crosstalk and improving the bone regeneration microenvironment by the SC-exos@G/S construct is a straightforward and effective strategy for neurovascularized bone regeneration.

4. Conclusion

In conclusion, this study indicates that SCs are critical cells originating from the peripheral nervous system that participate in bone repair, secreting exosomes to the microenvironment for regulating bone regeneration. Furthermore, this study shows that SC-exos can regulate the TGFβ signaling pathway to promote the osteogenic differentiation of BMSCs by transferring let-7c-5p. Moreover, the SC-exos@G/S constructs, which are developed using bioprinting technology, are able to simulate SC-mediated nerve–bone crosstalk, improve the bone regeneration microenvironment, and thus promote effective bone repair. Our study highlights the pivotal role of SC-exos in the regulation of SCs for the bone regeneration microenvironment and provides a new strategy for tissue engineering constructs that promote neurovascularized bone regeneration by enhancing the regulatory effects of the nervous system. The strategy presented in this study may be an important approach for improving the repair effects of bone defects with neurological dysfunction.

5. Experimental section

5.1. Immunofluorescence of fracture sections

Rat femur fracture specimens from six-week-old SD rats were obtained at 14 d, fixed for 24 h in 4% paraformaldehyde, embedded in paraffin, and then sectioned for histological analysis. The manufacturer's instructions were followed for staining various immunofluorescent proteins. The S100β (1:1000, GB12359; Servicebio, Wuhan, China) and β III-tubulin (1:1000, GB12139; Servicebio, Wuhan, China) specific primary antibodies were used in this work. Fluorescein isothiocyanate (FITC)-conjugated goat anti-mouse IgG (1:400, GB25301, Servicebio, Wuhan, China) or cy5-conjugated goat anti-rabbit IgG (GB27303, Servicebio, Wuhan, China) was used as the secondary antibody and incubated at 25 °C for 2 h before being combined with DAPI for co-incubation at 25 °C.

5.2. Cell isolation and culture

BMSCs were isolated from the bone marrow cavity of the bilateral femurs of four-week-old SD rats according to previous studies [62,63]. Briefly, the animals were sacrificed by euthanizing, and their skeletons were rinsed using 70% ethanol. The hind limbs were harvested for further dissection to obtain the tibia and femur. Ice-cold PBS with 1 × penicillin–streptomycin was used to rinse the bone tissue three times. A sharp blade was used to cut the ends of the tibia and femur to expose the marrow cavity. Then the marrow was flushed out of the marrow cavity using a 1 mL syringe containing α-MEM and collected in a 10 cm culture dish on ice. A 70 mm filter mesh was used to remove any bone spicules or muscle and cell clumps to get the cell suspension. Finally, the cell suspension was cultured with α- MEM supplemented with 10% (v/v) fetal bovine serum (FBS) and 1% (v/v) penicillin–streptomycin at 37 °C with 5% CO_2. The medium was replaced with fresh complete medium every 3 d. For use in subsequent investigations, cells were passaged to P3–P5.

EPCs were also isolated from the bone marrow cavity of the bilateral femurs of four-week-old SD rats according to previous studies [64,65]. The flushing procedure of bone marrow extracts was the same as the BMSC isolation. After incubating the cell suspension for 4 h, non-adherent cells that accumulated on the surface of the culture dish were pipetted into a new culture dish. Then the EGM-2MV (Lonza Group, CH) was added to culture primary EPCs. The medium was replaced with fresh complete medium every 3 d. For use in subsequent investigations, cells were passaged to P3–P5.

SCs were isolated from the bilateral sciatic nerves of four-week-old SD rats according to previous studies [66,67]. Briefly, 70% ethanol was used to disinfect the skin area of the hind limb. Next, fine surgical scissors were used to make an incision in the posterolateral hind limb area. The sciatic nerve was carefully isolated from the posterior femur muscle group. Then, the most proximal and distal end of the nerve were cut using fine surgical scissors. The isolated sciatic nerves were collected and rinsed with ice PBS three times. Next, the scissors were used to remove the epineurium layer for harvesting individual fibers. Finally, the nerve fibers were collected for enzymatic dissociation with an enzymatic cocktail solution composed of 0.125% trypsin and 0.2% type I collagenase at 37 °C. After termination of enzymatic dissociation, the primary SCs were grown at 37 °C with 5% CO_2 in high-glucose Dulbecco's Modified Eagle Medium (DMEM) with 10% FBS, 1% (v/v) penicillin–streptomycin, 2 μM forskolins (MCE, USA), and 2 ng mL^{-1} recombinant human neuregulin (R&D, USA). For use in subsequent investigations, cells were passaged to P3–P5.

5.3. Effect of SCs on BMSCs by paracrine signaling

To provide the conditioned medium for the culture of BMSCs, the SC supernatant from the P3–P5 generation was collected, filtered through a 0.22 m filter (Merck Millipore, Burlington, MA), and combined with α-MEM at predetermined mixing ratios of 10%, 30%, and 50%. Every 3 d, the culture medium was replaced. SCs were primed with either GW4869 (MCE, USA) or PBS to determine the function of exosomes in SC paracrine signaling. The supernatant was then collected, diluted with α-MEM at a 1:1 ratio, and utilized as the conditioned medium for BMSC culture. Every 3 d, the culture medium was replaced. The qRT-PCR assay was used to monitor gene expression involved in osteogenic differentiation (ALP, Runx-2, OCN, OPN, and OSX). The CCK-8 test was employed to monitor cell proliferation. Western blot and immunofluorescence staining were performed to detect the expression of osteogenesis-related proteins (Runx-2 and OPN).

5.4. Isolation and identification of exosomes

In this investigation, exosome production was carried out using SCs in passages 3–5. After reaching 80–90% confluence, the medium was removed, and the cells were washed three times in PBS and resuspended in a traditional medium with 10% exosomes-depleted FBS. Exosomes were isolated and purified using the gradient low-temperature ultracentrifugation method, which was well documented in the literature after 24–48 h of culture. The supernatant was first filtered through a 0.22 μm filter to remove suspended cells and centrifuged at 10,000×*g* for 30 min at 4 °C to remove cell debris and finally at 100,000×*g* for 70 min at 4 °C to recover the exosomes [68]. The exosome pellet was cleared, resuspended in 100 μL PBS, and stored at −80 °C for future research. TEM was used to analyze the morphology of the exosome. After being air-dried, the exosome solution was embedded in a TEM grid of a skinny carbon layer. ZetaView (Particle Metrix) was used for the NTA to evaluate the particle size of exosomes. A BCA protein assay kit (Beyotime, Jiangsu, China) was used to assess the concentration of exosomes. Exosome-related markers and primary antibodies including CD9, HSP70, and TSG101 were detected using Western blot analysis.

5.5. Internalization experiment

ExoSparker Exosome Membrane Labeling Kit-Green (Dojindo, Japan) was used to stain the isolated exosomes according to the manufacturer's instructions. The BMSCs received 10 μg of the dye-labeled exosomes, which were then incubated for 0, 4, and 8 h at 37 °C with 5% CO_2. The cells were then fixed with 4% paraformaldehyde for 15 min after being rinsed with PBS to eliminate exosomes that were not absorbed by the cells. The cells were stained for cytoskeleton and nuclear staining with tetramethylrhodamine B isothiocyanate (TRITC)–phalloidin for 2 h at room temperature and DAPI for 10 min at room temperature, respectively. Confocal laser scanning microscopy (Leica, Germany) was used to visualize exosomes internalized by BMSCs at

different points.

5.6. Effect of SC-exos on BMSCs

SC-exos were co-cultured with BMSCs at concentrations of 0 (PBS), 1, 10, and 100 μg mL^{-1} to determine the impact of SC-exos on BMSCs. Every 3 d, the culture medium was replaced. Cell proliferation was evaluated using the CCK-8 assay. To assess the osteogenic function of BMSCs in vitro, ALP staining (P0321S, Beyotime, Jiangsu, China) and Alizarin Red S staining (C0138, Beyotime, Jiangsu, China) were conducted using the according to the manufacturer's instructions. The expression levels of genes (ALP, Runx-2, OCN, OPN, and OSX) involved in osteogenic differentiation were determined using real-time PCR, and the osteogenesis-related markers (Runx-2 and OPN) were detected using Western blot.

5.7. Exosomal microRNAs sequencing and bioinformatic analysis

OE Biotech Co. Ltd. performed mini RNA-seq on SCs and their exosomes (Shanghai, China). By using the manufacturer's instructions, total RNA was isolated from the three sets of SCs and SC-exos using the mirVana miRNA Isolation Kit (Ambion), and the integrity of the RNA was determined using an Agilent 2100 Bioanalyzer (Agilent Technology, USA).

The adapter-ligated RNAs were further processed after reverse transcription by cDNA and PCR amplification. Small RNA libraries were created from extracted and purified PCR products with sizes between 140 and 160 bp. An Agilent Bioanalyzer 2100 system with DNA High Sensitivity Chips was used to evaluate the quality of the library. Libraries were sequenced using the Illumina HiSeq X Ten platform. Then, 150 bp paired-end readings were produced. $|\log2 \text{ (fold change)}| \geq 1$ and $p < 0.05$ were determined to indicate differential expression.

5.8. Bioinformatic analysis and target gene prediction

To confirm the miR quality and consistency among the three SCs/SC-exos samples, total small RNA from SCs and SC-exos samples were analyzed for known and unknown RNA, miRNA upset analysis, CPM gene expression density distribution, and correlation analysis of samples. Based on the hypergeometric distribution, the top 30 highly expressed miRNA-target genes underwent GO and KEGG pathway enrichment analyses.

5.9. Luciferase report assay

Using Lipofectamine 3000, cells were co-transfected with luciferase vectors expressing miR-let-7c-5p mimics or mimics-NC and the wild-type or mutant 3′-UTR of Acvr1b (Invitrogen). At 48 h after transfection, luciferase activity was assessed using a dual-luciferase reporter assay kit (Beyotime, Jiangsu, China).

5.10. Molecular mechanism analysis of the effect of let-7c-5p on BMSCs

Using Lipofectamine RNAiMAX (Invitrogen, USA), mimics of let-7c into BMSCs according to the manufacturer's instructions to investigate the underlying mechanism of miRNAs. The BMSCs were transfected upon reaching 50% confluence. In brief, Lipofectamine RNAiMAX was combined with miRNA mimics in OPTI-MEM reduced serum medium, and the mixture was incubated at room temperature for 5 min before transfection. The transfection mixture was then added to the BMSCs, and the combination was incubated at 37 °C for 8 h without using a dual antibody in α-MEM medium supplemented with 10% FBS. The culture medium was changed to regular MEM with 10% FBS supplementation after 8 h. The supplementary information provides the miRNA mimic and inhibitor sequences. Utilizing poly(A)-tailed qRT-PCR, the transfection effectiveness of miRNA mimics or inhibitors was assessed after 48 h (B532451, Sangon Biotech, China). Using qRT-PCR and immunofluorescence staining to detect the expression of genes and proteins associated with osteogenesis. The Acvr1b protein and expression of Smad and phosphorylated Smad proteins (Smad1, pSmad1, Smad2, and pSmad2) were examined using Western blot assay. Acvr1b (1:200, 10086, Proteintech, China), Smad1 (1:1000, 10429, Proteintech, China), pSmad1 (1:1000, 9516S, CST, USA), Smad2 (1:1000, 5339T, CST, USA), and pSmad2 (1:1000, 3108S, CST, USA) were the primary targets of the antibodies.

5.11. Bioink preparation

Briefly, a serum-free medium was used to dissolve GelMA and SilMA (both from EFL, Suzhou, China). After 0.5 wt% of a visible light initiator was added, the solution was incubated at 45 °C until the solids were completely dissolved. A 0.22 μm filter was used to filter-sterilize the solution. The combined hydrogel was mixed with isolated exosomes (100 μg mL^{-1}) to prepare a pre-hydrogel solution. The pre-hydrogel solution was repeatedly pipetted and mixed before being placed in a centrifuge tube, centrifuged at 300×*g* for 5 min to eliminate air bubbles, and then incubated at 37 °C to prepare for printing. During bioprinting, the BMSCs and SC-exos (100 μg mL^{-1}) were mixed with the pre-hydrogel according to a cell volume of 1×10^7 cells mL^{-1} and then transferred to the cartridge for bioprinting after being evenly pipetted.

5.12. Bioprinting and biocompatibility assay

The bioprinting process was carried out using a triaxial bioprinting machine (Regenvo Biotechnology, Hangzhou, China). Before use, the printing apparatus was set up on a spotless bench and sanitized using 75% alcohol and UV light. Tools for bioprinting, including cartridges, needles (27G), and tweezers, were autoclaved at 121 °C for 2 h before use. A layer-by-layer grid-like structure (10 mm × 10 mm × 2 mm) was created using SOLIDWORKS as a bioprinting model.

The printing parameters were as follows: wire diameter, 200 μm; wire spacing, 200 μm; air pressure, 0.2 kPa; printing nozzle temperature, 25 °C; platform temperature, 20 °C. The bioprinted constructs were photocrosslinked using a UV light for 2 min and then transferred to a 12-well plate for subsequent culture in an incubator with α-MEM supplemented with 10% FBS at 37 °C under 5% CO_2.

The biocompatibility assay of biopronted constructs was performed by live/dead staining, EdU staining experiment, and the staining of the cytoskeleton. The live/dead staining was performed using a live/dead cell staining kit according to the manufacturer's instructions (KeyGEN, Nanjing, China) at 4 and 24 h after printing, as well as at 3 and 7 d for culture. The samples were observed using a laser scanning confocal microscope (Leica, Germany). Calcein AM-stained live (green) cells were detected with excitation at 488 nm, and PI-stained dead (red) cells were observed with excitation at 555 nm.

The EdU staining experiment was performed to assess the proliferation of BMSCs in the bio-scaffolds at 3 d after printing following the manufacturer's instructions. The samples were incubated in EdU working solution for 30 min, followed by staining of nuclei with DAPI (Solarbio, China) for 5 min. Then, the samples were observed with a laser scanning confocal microscope (Leica, Germany).

In order to observe the morphology of cells in the scaffolds, the samples were fixed with 4% paraformaldehyde at 14 d after printing, then stained with phalloidin-FITC (Kingmorn, China) for 1 h, and the nuclei were stained with DAPI for 5 min. The samples were observed using a laser scanning confocal microscope (Leica, Germany).

5.13. Rheology analysis

The rheological characteristics of the hybrid hydrogels were evaluated using a rheometer (MCR302, Anton Paar, Austria) with a Peltier element for temperature regulation. Viscosity and shear stress were

observed by raising the shear rate from 1 s^{-1} to 500 s^{-1} at a rate of 0.08 s^{-1} at 25 °C. The hydrogel samples were equilibrated at 40 °C and subsequently cooled at a rate of 1 °C min^{-1} from 35 °C to 15 °C while the storage (G') and loss moduli (G'') were determined at a constant frequency of 1 Hz and under a persistent strain of 0.1%.

5.14. Scanning electron microscopy

The samples were freeze-dried after being treated in glutaraldehyde for 1 h at room temperature. Then, a scanning electron microscope (Sirion 200, FEI, USA) was used to observe the surface morphologies of the bioprinted constructions.

5.15. Exosome release analysis

To detect the release ratio of exosomes in the hybrid hydrogel, hybrid hydrogels were prepared in three proportions (10% GelMA, 8/2% GelMA/SilMA, and 6/4% GelMA/SilMA); then, the exosomes were added to the hybrid hydrogels at 100 μg mL^{-1}. The exosome release rate from the hybrid hydrogels was assessed using the BCA kit according to the manufacturer's directions after exposing the hybrid hydrogels to UV light for 2 min to create chemical crosslinks. In a 24-well plate (Transwell), 600 μL of PBS was poured into the lower chamber, and the mixed hydrogel block was placed in the upper chamber. Then, 100 μL of PBS in the lower chamber was aspirated and replaced with fresh PBS at predetermined intervals. The quantity and proportion of the exosomes that were released were calculated. Data were presented as the means and standard deviations of three replicates.

5.16. Detection of osteogenic property of bioprinted constructs

Immunofluorescence and qRT-PCR tests were conducted to determine whether the bioprinted constructs exhibited osteogenic qualities after being cultured in vitro for 7 d. The cells were treated for immunofluorescence by being washed three times with PBS, fixed for 15 min in 4% paraformaldehyde, and then incubated overnight with Runx2 (1:1600, 12556, CST, USA) and OPN (1:1600, ab8448, Abcam, UK) antibodies. Cytoskeleton staining was carried out using goat anti-rabbit IgG H&L (1:1000, ab150117, Abcam, UK) that was Alexa Fluor 488-labeled for 2 h at room temperature, followed by TRITC–phalloidin for 30 min at room temperature. The nuclei were then stained with DAPI for a final 5 min at room temperature. The bioprinted constructs were divided up for qRT-PCR, and total RNA was extracted using the Trizol technique for searching gene expression in osteogenesis.

5.17. Subcutaneous implant

This study followed the recommendations of the Shanghai Ninth People's Hospital, Shanghai Jiaotong University School of Medicine's Animal Care and Experimentation Committee. Twelve 8-week-old rats from the G/S and SC-exos@G/S groups were used in this study. Each rat received four bioprinted constructs inserted subcutaneously on the dorsal side. The implants and surrounding tissues were removed, fixed in 4% paraformaldehyde for 2 h, embedded in paraffin, and sectioned when the rats were euthanized after two weeks. In this experiment, 6 μm thick slices were used for histological analysis. Bone, vascular, and nerve structures were detected using HE and immunofluorescence staining. For immunofluorescence, OCN (1:200, GB11233, Servicebio, Wuhan, China), CD31 (1:200, GB12063, Servicebio, Wuhan, China), α-SMA (1:200, GB111364, Servicebio, Wuhan, China), NF200 (1:500, GB12144, Servicebio, Wuhan, China), or MBP antibodies (1:200, GB11226, Servicebio, Wuhan, China) were incubated overnight at 4 °C. Cy5-conjugated goat anti-rabbit IgG (1:500, GB27303, Servicebio, Wuhan, China) or FITC-conjugated goat antibody rabbit IgG (1:500, GB22303, Servicebio, Wuhan, China) was used as secondary antibody, incubated for 2 h at room temperature, and stained with DAPI for 5 min at room temperature. Before the animals were slaughtered, ultrasonography (VEVO LAZR-X; Fujifilm VisualSonics, USA) was conducted to evaluate blood perfusion.

5.18. Scratch and tube formation assay

Scratch experiments to further investigate the effect of SC-exos on the migration of EPCs. EPCs were seeded in a six-well plate with 2×10^5 cells. When the cell confluence reached 90%, a 200 μL pipette tip was used to create a linear wound which was washed three times with PBS to remove dead cells and cell debris. Then, DMEM containing 3% exosome-depleted FBS and specific doses of exosomes (0, 1, 10, and 100 μg mL^{-1}) were added, and cells were observed using light microscopy at 0, 12 and 24 h after scratching and photographed.

EPCs were pretreated with specific concentrations of SC-exos (0, 1, 10, and 100 μg mL^{-1}) overnight, seeded 2×10^4 cells per well in 48-well plates pretreated with Matrigel, incubated for 6 h in a cell incubator at 37 °C under 5% CO_2. Then observed and photographed using a microscope. ImageJ was used to measure the total number of branches and connection points. All experiments were repeated at least three times.

5.19. Surgical procedure

The Institutional Animal Care and Use Committee of Shanghai Ninth People's Hospital prepared guidelines for all animal research. The Ethics Committee of Shanghai Ninth People's Hospital examined and approved the protocols.

To assess the promoting effect of bioprinted constructs on bone regeneration, a critical-sized calvarial lesion model was established in 8-week-old male SD rats (weighing 200–220 g). Pentobarbital (3.5 mg/100 g) was administered intraperitoneally to the animals to render them unconscious. An incision of 1 cm length was made on the rat's scalp, and the skull was then exposed through blunt dissection. A 6 mm diameter low-speed hole drill was used to create two full-thickness flaws on either side of the rat skull, and the holes were subjected to different treatments. The rats were split into four groups: the control group, which was not treated; the G/S group, which was implanted with the G/S constructs; the Exo group, which was treated using a direct one-time in-situ injection of large doses of SC-exos (100 μg mL^{-1}); and the SC-exos@G/S group, which was implanted with the SC-exos@G/S. The experiment involved the analysis of six samples per group. Eight weeks following surgery, the rats were slaughtered, and the tissues were preserved using 4% paraformaldehyde. The samples were scanned using a micro-CT machine (CT80; Scanco, Switzerland). Decalcified samples were prepared for further histological examination after approximately 30 d of immersion in a 20% ethylene diamine tetraacetic acid (EDTA) solution. The manufacturer's directions were followed for applying HE and Masson's trichrome staining.

5.20. Statistical analysis

The results were expressed as mean ± standard deviation (SD). All data were analyzed in more than three independent experiments. Student's t-test and one-way ANOVA were used for statistical analysis. Statistical significance was set at $^*p < 0.05$.

Ethics approval and consent to participate

The use of rats and all related procedures in this study were approved by the Animal Care and Use Committee of Shanghai Ninth People's Hospital, Shanghai Jiao Tong University School of Medicine and were carried out in accordance with the guidelines of the National Institutes of Health Guide for Care and Use of Laboratory Animals (No. GB14925-2010).

CRediT authorship contribution statement

Tianchang Wang: Writing – original draft, Validation, Formal analysis, Visualization, Software, Methodology, Investigation. **Wentao Li:** Data curation, Methodology, Investigation. **Yuxin Zhang:** Visualization, Software, Methodology. **Xiang Xu:** Writing – review & editing. **Lei Qiang:** Investigation. **Weiqiang Miao:** Investigation. **Xiaokun Yue:** Formal analysis. **Xin jiao:** Formal analysis. **Xianhao Zhou:** Software. **Zhenjiang Ma:** Formal analysis. **Shuai Li:** Formal analysis. **Muliang Ding:** Software. **Junfeng Zhu:** Formal analysis. **Chi Yang:** Formal analysis. **Hui Wang:** Data curation. **Tao Li:** Supervision, Validation, Writing – review & editing. **Xin Sun:** Visualization, Supervision, Validation, Writing – review & editing. **Jinwu Wang:** Supervision, Validation, Writing – review & editing, Project administration, Funding acquisition.

Declaration of competing interest

The authors declare that there is no conflict of interests.

Acknowledgements

The authors appreciate financial support from National Key R&D Program of China (2018YFA0703000), National Natural Science Foundation of China (82072412), Translation Medicine National Key Science and Technology Infrastructure (Shanghai) Open Project (TMSK-2020-118), Lingang Laboratory “Seeking Outstanding Youth Program” open project (LG-QS-202206-04). Thanks to Dr. W. Wang for your help in writing this article.

Appendix A. Supplementary data

Supplementary data to this article can be found online at https://doi.org/10.1016/j.bioactmat.2023.02.013.

References

[1] X. Zhang, X. Jiang, S. Jiang, X. Cai, S. Yu, G. Pei, Schwann cells promote prevascularization and osteogenesis of tissue-engineered bone via bone marrow mesenchymal stem cell-derived endothelial cells, Stem Cell Res. Ther. 12 (1) (2021) 382.
[2] R. Dimitriou, E. Jones, D. McGonagle, P.V. Giannoudis, Bone regeneration: current concepts and future directions, BMC Med. 9 (2011) 66.
[3] J. Cao, S. Zhang, A. Gupta, Z. Du, D. Lei, L. Wang, X. Wang, Sensory nerves affect bone regeneration in rabbit mandibular distraction osteogenesis, Int. J. Med. Sci. 16 (6) (2019) 831–837.
[4] Z. Li, C.A. Meyers, L. Chang, S. Lee, Z. Li, R. Tomlinson, A. Hoke, T.L. Clemens, A. W. James, Fracture repair requires TrkA signaling by skeletal sensory nerves, J. Clin. Invest. 129 (12) (2019) 5137–5150.
[5] R.E. Tomlinson, Z. Li, Q. Zhang, B.C. Goh, Z. Li, D.L.J. Thorek, L. Rajbhandari, T. M. Brushart, L. Minichiello, F. Zhou, A. Venkatesan, T.L. Clemens, NGF-TrkA signaling by sensory nerves coordinates the vascularization and ossification of developing endochondral bone, Cell Rep. 16 (10) (2016) 2723–2735.
[6] A. Salhotra, H.N. Shah, B. Levi, M.T. Longaker, Mechanisms of bone development and repair, Nat. Rev. Mol. Cell Biol. 21 (11) (2020) 696–711.
[7] N. Liu, Y. Zhu, K. Yu, Z. Gu, S. Lv, Y. Chen, C. He, J. Fu, Y. He, Functional blood-brain barrier model with tight connected minitissue by liquid substrates culture, Adv. Healthc. Mater. 12 (4) (2023), e2201984.
[8] P.X. Zhang, X.R. Jiang, L. Wang, F.M. Chen, L. Xu, F. Huang, Dorsal root ganglion neurons promote proliferation and osteogenic differentiation of bone marrow mesenchymal stem cells, Neural Regen Res 10 (1) (2015) 119–123.
[9] X.D. Wang, S.Y. Li, S.J. Zhang, A. Gupta, C.P. Zhang, L. Wang, The neural system regulates bone homeostasis via mesenchymal stem cells: a translational approach, Theranostics 10 (11) (2020) 4839–4850.
[10] R. Chen, Z. Hao, X. Chen, Q. Fu, Y. Ma, Neuropeptide Y enhances proliferation and chondrogenic differentiation of ATDC5 cells, Neuropeptides 80 (2020), 102022.
[11] S. Sun, N.H. Diggins, Z.J. Gunderson, J.C. Fehrenbacher, F.A. White, M.A. Kacena, No pain, no gain? The effects of pain-promoting neuropeptides and T neurotrophins on fracture healing, Stem Cell. Dev. 131 (2020), 115109.
[12] W.T. Li, W.Q. Miao, Y.H. Liu, T.C. Wang, Y.X. Zhang, W.H. Wang, D.Z. Lu, X. H. Zhou, X. Jiao, X.L. Jia, Y.X. Lin, Y.C. Li, H.T. He, Y.Q. Mao, Z.J. Ma, T. Li, J. W. Wang, Bioprinted constructs that mimic the ossification center microenvironment for targeted innervation in bone regeneration, Adv. Funct. Mater. 32 (9) (2022).
[13] R. Lopez-Leal, F.A. Court, Schwann cell exosomes mediate neuron-glia communication and enhance axonal regeneration, Cell. Mol. Neurobiol. 36 (3) (2016) 429–436.
[14] S. Stierli, V. Imperatore, A.C. Lloyd, Schwann cell plasticity-roles in tissue homeostasis, regeneration, and disease, Glia 67 (11) (2019) 2203–2215.
[15] A.P. Johnston, S.A. Yuzwa, M.J. Carr, N. Mahmud, M.A. Storer, M.P. Krause, K. Jones, S. Paul, D.R. Kaplan, F.D. Miller, Dedifferentiated Schwann cell precursors secreting paracrine factors are required for regeneration of the mammalian digit tip, Cell Stem Cell 19 (4) (2016) 433–448.
[16] R.E. Jones, A. Salhotra, K.S. Robertson, R.C. Ransom, D.S. Foster, H.N. Shah, N. Quarto, D.C. Wan, M.T. Longaker, Skeletal stem cell-Schwann cell circuitry in mandibular repair, Cell Rep. 28 (11) (2019) 2757–2766 e5.
[17] R. Kalluri, V.S. LeBleu, The biology, function, and biomedical applications of exosomes, Science 367 (6478) (2020).
[18] R. Isaac, F.C.G. Reis, W. Ying, J.M. Olefsky, Exosomes as mediators of intercellular crosstalk in metabolism, Cell Metabol. 33 (9) (2021) 1744–1762.
[19] H. Valadi, K. Ekstrom, A. Bossios, M. Sjostrand, J.J. Lee, J.O. Lotvall, Exosome-mediated transfer of mRNAs and microRNAs is a novel mechanism of genetic exchange between cells, Nat. Cell Biol. 9 (6) (2007), 654-U72.
[20] C.C. Huang, R. Narayanan, S. Alapati, S. Ravindran, Exosomes as biomimetic tools for stem cell differentiation: applications in dental pulp tissue regeneration, Biomaterials 111 (2016) 103–115.
[21] X.Q. Wang, O. Omar, F. Vazirisani, P. Thomsen, K. Ekstrom, Mesenchymal stem cell-derived exosomes have altered microRNA profiles and induce osteogenic differentiation depending on the stage of differentiation, PLoS One 13 (2) (2018).
[22] M.A. Lopez-Verrilli, F. Picou, F.A. Court, Schwann cell-derived exosomes enhance axonal regeneration in the peripheral nervous system, Glia 61 (11) (2013) 1795–1806.
[23] R. Lopez-Leal, F. Diaz-Viraque, R.J. Catalan, C. Saquel, A. Enright, G. Iraola, F. A. Court, Schwann cell reprogramming into repair cells increases miRNA-21 expression in exosomes promoting axonal growth, J. Cell Sci. 133 (12) (2020).
[24] Z. Wu, P. Pu, Z. Su, X. Zhang, L. Nie, Y. Chang, Schwann Cell-derived exosomes promote bone regeneration and repair by enhancing the biological activity of porous Ti6Al4V scaffolds, Biochem. Biophys. Res. Commun. 531 (4) (2020) 559–565.
[25] Y. Su, Q. Gao, R. Deng, L. Zeng, J. Guo, B. Ye, J. Yu, X. Guo, Aptamer engineering exosomes loaded on biomimetic periosteum to promote angiogenesis and bone regeneration by targeting injured nerves via JNK3 MAPK pathway, Mater Today Bio 16 (2022), 100434.
[26] Z. Hao, L. Ren, Z. Zhang, Z. Yang, S. Wu, G. Liu, B. Cheng, J. Wu, J. Xia, A multifunctional neuromodulation platform utilizing Schwann cell-derived exosomes orchestrates bone microenvironment via immunomodulation, angiogenesis and osteogenesis, Bioact. Mater. 23 (2023) 206–222.
[27] P.S. Gungor-Ozkerim, I. Inci, Y.S. Zhang, A. Khademhosseini, M.R. Dokmeci, Bioinks for 3D bioprinting: an overview, Biomater. Sci. 6 (5) (2018) 915–946.
[28] S.V. Murphy, A. Atala, 3D bioprinting of tissues and organs, Nat. Biotechnol. 32 (8) (2014) 773–785.
[29] X. Sun, Z. Ma, X. Zhao, W. Jin, C. Zhang, J. Ma, L. Qiang, W. Wang, Q. Deng, H. Yang, J. Zhao, Q. Liang, X. Zhou, T. Li, J. Wang, Three-dimensional bioprinting of multicell-laden scaffolds containing bone morphogenic protein-4 for promoting M2 macrophage polarization and accelerating bone defect repair in diabetes mellitus, Bioact. Mater. 6 (3) (2021) 757–769.
[30] S. Vijayavenkataraman, W.C. Yan, W.F. Lu, C.H. Wang, J.Y.H. Fuh, 3D bioprinting of tissues and organs for regenerative medicine, Adv. Drug Deliv. Rev. 132 (2018) 296–332.
[31] Z. Ding, W. Cheng, M.S. Mia, Q. Lu, Silk biomaterials for bone tissue engineering, Macromol. Biosci. 21 (8) (2021), e2100153.
[32] J. Melke, S. Midha, S. Ghosh, K. Ito, S. Hofmann, Silk fibroin as biomaterial for bone tissue engineering, Acta Biomater. 31 (2016) 1–16.
[33] F. Mottaghitalab, H. Hosseinkhani, M.A. Shokrgozar, C.B. Mao, M.Y. Yang, M. Farokhi, Silk as a potential candidate for bone tissue engineering, J. Contr. Release 215 (2015) 112–128.
[34] P. Bhattacharjee, B. Kundu, D. Naskar, H.W. Kim, T.K. Maiti, D. Bhattacharya, S. C. Kundu, Silk scaffolds in bone tissue engineering: an overview, Acta Biomater. 63 (2017) 1–17.
[35] V. Fitzpatrick, Z. Martin-Moldes, A. Deck, R. Torres-Sanchez, A. Valat, D. Cairns, C. Li, D.L. Kaplan, Functionalized 3D-printed silk-hydroxyapatite scaffolds for enhanced bone regeneration with innervation and vascularization, Biomaterials 276 (2021), 120995.
[36] E. Pishavar, H.R. Luo, M. Naserifar, M. Hashemi, S. Toosi, A. Atala, S. Ramakrishna, J. Behravan, Advanced hydrogels as exosome delivery systems for osteogenic differentiation of MSCs: application in bone regeneration, Int. J. Mol. Sci. 22 (12) (2021).
[37] C. Han, J. Zhou, B. Liu, C. Liang, X. Pan, Y. Zhang, Y. Zhang, Y. Wang, L. Shao, B. Zhu, J. Wang, Q. Yin, X.Y. Yu, Y. Li, Delivery of miR-675 by stem cell-derived exosomes encapsulated in silk fibroin hydrogel prevents aging-induced vascular dysfunction in mouse hindlimb, Mater Sci Eng C Mater Biol Appl 99 (2019) 322–332.
[38] K. Shen, A. Duan, J. Cheng, T. Yuan, J. Zhou, H. Song, Z. Chen, B. Wan, J. Liu, X. Zhang, Y. Zhang, R. Xie, F. Liu, W. Fan, Q. Zuo, Exosomes derived from hypoxia preconditioned mesenchymal stem cells laden in a silk hydrogel promote cartilage regeneration via the miR-205-5p/PTEN/AKT pathway, Acta Biomater. 143 (2022) 173–188.
[39] M.J. Carr, A.P.W. Johnston, Schwann cells as drivers of tissue repair and regeneration, Curr. Opin. Neurobiol. 47 (2017) 52–57.

[40] A.I. Mahmoud, C.C. O'Meara, M. Gemberling, L. Zhao, D.M. Bryant, R. Zheng, J. B. Gannon, L. Cai, W.Y. Choi, G.F. Egnaczyk, C.E. Burns, C.G. Burns, C.A. MacRae, K.D. Poss, R.T. Lee, Nerves regulate cardiomyocyte proliferation and heart regeneration, Dev. Cell 34 (4) (2015) 387–399.
[41] P.J. Apel, D. Crane, C.N. Northam, M. Callahan, T.L. Smith, R.D. Teasdall, Effect of selective sensory denervation on fracture-healing: an experimental study of rats, J Bone Joint Surg Am 91 (12) (2009) 2886–2895.
[42] T. Itoyama, S. Yoshida, A. Tomokiyo, D. Hasegawa, S. Hamano, H. Sugii, T. Ono, S. Fujino, H. Maeda, Possible function of GDNF and Schwann cells in wound healing of periodontal tissue, J. Periodontal. Res. 55 (6) (2020) 830–839.
[43] B. Chen, G.-x. Pei, D. Jin, K.-h. Wei, Y. Qin, Q.-s. Liu, Distribution and property of nerve fibers in human long bone tissue, 01, Chin. J. Traumatol. 10 (2007) 3–9.
[44] D.B. Mach, S.D. Rogers, M.C. Sabino, N.M. Luger, M.J. Schwei, J.D. Pomonis, C. P. Keyser, D.R. Clohisy, D.J. Adams, P. O'Leary, P.W. Mantyh, Origins of skeletal pain: sensory and sympathetic innervation of the mouse femur, Neuroscience 113 (1) (2002) 155–166.
[45] J.M. Spinazzola, E. Gussoni, Exosomal small talk carries Strong messages from muscle stem cells, Cell Stem Cell 20 (1) (2017) 1–3.
[46] Z. Shu, J. Tan, Y. Miao, Q. Zhang, The role of microvesicles containing microRNAs in vascular endothelial dysfunction, J. Cell Mol. Med. 23 (12) (2019) 7933–7945.
[47] Y. Zhang, Y. Xie, Z. Hao, P. Zhou, P. Wang, S. Fang, L. Li, S. Xu, Y. Xia, Umbilical mesenchymal stem cell-derived exosome-encapsulated hydrogels accelerate bone repair by enhancing angiogenesis, ACS Appl. Mater. Interfaces 13 (16) (2021) 18472–18487.
[48] G. Chen, C. Deng, Y.P. Li, TGF-beta and BMP signaling in osteoblast differentiation and bone formation, Int. J. Biol. Sci. 8 (2) (2012) 272–288.
[49] X. Guo, X.F. Wang, Signaling cross-talk between TGF-beta/BMP and other pathways, Cell Res. 19 (1) (2009 Jan) 71–88, https://doi.org/10.1038/cr.2008.302. PMID: 19002158; PMCID: PMC3606489.
[50] O.E. Olsen, K.F. Wader, H. Hella, A.K. Mylin, I. Turesson, I. Nesthus, A. Waage, A. Sundan, T. Holien, Activin A inhibits BMP-signaling by binding ACVR2A and ACVR2B, Cell Commun. Signal. 13 (2015) 27.
[51] J.W. Lowery, D. Pazin, G. Intini, S. Kokabu, V. Chappuis, L.P. Capelo, V. Rosen, The role of BMP2 signaling in the skeleton, Crit. Rev. Eukaryot. Gene Expr. 21 (2) (2011) 177–185.
[52] Y. Matsumoto, F. Otsuka, J. Hino, T. Miyoshi, M. Takano, M. Miyazato, H. Makino, K. Kangawa, Bone morphogenetic protein-3b (BMP-3b) inhibits osteoblast differentiation via Smad2/3 pathway by counteracting Smad1/5/8 signaling, Mol. Cell. Endocrinol. 350 (1) (2012) 78–86.
[53] S.J. Hatsell, V. Idone, D.M. Wolken, L. Huang, H.J. Kim, L. Wang, X. Wen, K. C. Nannuru, J. Jimenez, L. Xie, N. Das, G. Makhoul, R. Chernomorsky, D. D'Ambrosio, R.A. Corpina, C.J. Schoenherr, K. Feeley, P.B. Yu, G. D. Yancopoulos, A.J. Murphy, A.N. Economides, ACVR1R206H receptor mutation causes fibrodysplasia ossificans progressiva by imparting responsiveness to activin A, Sci. Transl. Med. 7 (303) (2015), 303ra137.
[54] S.H. Kim, Y.K. Yeon, J.M. Lee, J.R. Chao, Y.J. Lee, Y.B. Seo, M.T. Sultan, O.J. Lee, J. S. Lee, S.I. Yoon, I.S. Hong, G. Khang, S.J. Lee, J.J. Yoo, C.H. Park, Precisely printable and biocompatible silk fibroin bioink for digital light processing 3D printing, Nat. Commun. 9 (1) (2018) 1620.
[55] Q.Q. Wan, W.P. Qin, Y.X. Ma, M.J. Shen, J. Li, Z.B. Zhang, J.H. Chen, F.R. Tay, L. N. Niu, K. Jiao, Crosstalk between bone and nerves within bone, Adv. Sci. 8 (7) (2021).
[56] T. Wang, J. Cao, Z.J. Du, Y.B. Zhang, Y.P. Liu, L. Wang, D.L. Lei, Effects of sympathetic innervation loss on mandibular distraction osteogenesis, J. Craniofac. Surg. 23 (5) (2012) 1524–1528.
[57] J. Xue, J. Peng, M. Yuan, A. Wang, L. Zhang, S. Liu, M. Fan, Y. Wang, W. Xu, K. Ting, X. Zhang, S. Lu, NELL1 promotes high-quality bone regeneration in rat femoral distraction osteogenesis model, Bone 48 (3) (2011) 485–495.
[58] Y. Zhang, J. Xu, Y.C. Ruan, M.K. Yu, M. O'Laughlin, H. Wise, D. Chen, L. Tian, D. Shi, J. Wang, S. Chen, J.Q. Feng, D.H. Chow, X. Xie, L. Zheng, L. Huang, S. Huang, K. Leung, N. Lu, L. Zhao, H. Li, D. Zhao, X. Guo, K. Chan, F. Witte, H. C. Chan, Y. Zheng, L. Qin, Implant-derived magnesium induces local neuronal production of CGRP to improve bone-fracture healing in rats, Nat. Med. 22 (10) (2016) 1160–1169.
[59] D. Wang, Y. Lyu, Y. Yang, S. Zhang, G. Chen, J. Pan, W. Tian, Schwann cell-derived EVs facilitate dental pulp regeneration through endogenous stem cell recruitment via SDF-1/CXCR4 axis, Acta Biomater. 140 (2022) 610–624.
[60] Z. Li, Y. Liang, K. Pan, H. Li, M. Yu, W. Guo, G. Chen, W. Tian, Schwann cells secrete extracellular vesicles to promote and maintain the proliferation and multipotency of hDPCs, Cell Prolif 50 (4) (2017).
[61] V. Parfejevs, J. Debbache, O. Shakhova, S.M. Schaefer, M. Glausch, M. Wegner, U. Suter, U. Riekstina, S. Werner, L. Sommer, Injury-activated glial cells promote wound healing of the adult skin in mice, Nat. Commun. 9 (1) (2018) 236.
[62] M. Soleimani, S. Nadri, A protocol for isolation and culture of mesenchymal stem cells from mouse bone marrow, Nat. Protoc. 4 (1) (2009) 102–106.
[63] H. Zhu, Z.K. Guo, X.X. Jiang, H. Li, X.Y. Wang, H.Y. Yao, Y. Zhang, N. Mao, A protocol for isolation and culture of mesenchymal stem cells from mouse compact bone, Nat. Protoc. 5 (3) (2010) 550–560.
[64] T. Asahara, T. Murohara, A. Sullivan, M. Silver, R. van der Zee, T. Li, B. Witzenbichler, G. Schatteman, J.M. Isner, Isolation of putative progenitor endothelial cells for angiogenesis, Science 275 (5302) (1997) 964–967.
[65] X. Wang, Z. Zhao, H. Zhang, J. Hou, W. Feng, M. Zhang, J. Guo, J. Xia, Q. Ge, X. Chen, X. Wu, Simultaneous isolation of mesenchymal stem cells and endothelial progenitor cells derived from murine bone marrow, Exp. Ther. Med. 16 (6) (2018) 5171–5177.
[66] R. Mirsky, K.R. Jessen, Isolation of Schwann cell precursors from rodents, in: P. V. Monje, H.A. Kim (Eds.), Schwann Cells: Methods and Protocols, Springer New York, New York, NY, 2018, pp. 3–15.
[67] J. Kim, H.A. Kim, Isolation and expansion of Schwann cells from transgenic mouse models, in: P.V. Monje, H.A. Kim (Eds.), Schwann Cells: Methods and Protocols, Springer New York, New York, NY, 2018, pp. 39–48.
[68] C. Thery, S. Amigorena, G. Raposo, A. Clayton, Isolation and characterization of exosomes from cell culture supernatants and biological fluids, Curr Protoc Cell Biol Chapter 3 (2006). Unit 3 22.